Ferrando et al., 2020, Lithos 376-377, 105727, 1-18
doi: https://doi.org/10.1016/j.lithos.2020.105727
Post-print

Elsevier Editorial System(tm) for Lithos
Manuscript Draft

Manuscript Number: LITHOS8794R1

Title: Retrieving timescales of oceanic crustal evolution at Oceanic Core Complexes: Insights from diffusion modelling of geochemical profiles in olivine

Article Type: Regular Article

Keywords: lower oceanic crust at the Atlantis Massif; olivine trace elements; diffusive re-equilibration; oceanic crustal cooling; magma emplacement; exhumation by detachment faults

Corresponding Author: Mrs. Carlotta Ferrando,

Corresponding Author's Institution: University of Montpellier

First Author: Carlotta Ferrando

Order of Authors: Carlotta Ferrando; Kendra J Lynn, Ph.D.; Valentin Basch, Ph.D.; Benoit Ildefonse; Marguerite Godard

Abstract: The building of oceanic crust at Oceanic Core Complexes (OCC) has been described as a complex process involving multiple intrusions of magma over a protracted period of time. The migration of primitive magmas (i.e., Mid Ocean Ridge Basalts, MORBs) can lead to melt-rock interactions during reactive porous flow processes through the lithosphere. The timescales of these reactive processes and the subsequent cooling of the modified crystal matrix remain unconstrained. Diffusion modelling has been widely used to retrieve timescales of magmatic processes. In this study, we use diffusion models to constrain (i) the minimum timescales of melt-rock interactions and (ii) the cooling rates of the gabbroic sequence forming the oceanic crust at an OCC. We chose samples of the most primitive olivine-rich troctolites from the gabbroic sequence sampled in IODP Hole U1309D (Atlantis Massif OCC, Mid-Atlantic Ridge 30°N). Olivine-rich troctolites were interpreted as marking local partial assimilation of mantle intervals into the oceanic crust, and thus allowed to understand the dynamics of mantle assimilation and the formation of slow-spreading oceanic crust at the Atlantis Massif OCC. Olivines in olivine-rich troctolites represent relicts of pre-existing mantle olivine, while clinopyroxenes and plagioclases are crystallized during reactive percolation. Olivine chemical compositions show that olivine-rich troctolites inherit chemical heterogeneity from the mantle precursor. Flat geochemical profiles in olivine indicate complete chemical re-equilibration of olivine crystals with the locally modified percolating melt. Exception is made for most Ca profiles that show lower Ca contents at the olivine rim compared to the relative crystal core, as the result of subsolidus cooling. Three-dimensional (3D) diffusion models at magmatic conditions (T = 1210-1300°C and P = 2 kbar) reveal that complete chemical re-equilibration of 4 mm-size mantle-derived olivine with percolating MORB-type melts can be attained within durations of less than 300 yr. The Ca-in-olivine geospeedometer reveal that cooling rates from ~1200°C to ~1050°C are constant downhole and on average 0.004 °C/yr; they are comparable with lower temperature cooling rates (850°C-250°C) estimated at the Atlantis Massif OCC. The minimum timescales from 3D

models point to rather fast re-equilibration of olivine. The downhole chemical heterogeneity inherited from the precursor mantle, coupled with the timescales of diffusive re-equilibration suggest that the partial assimilation of the upwelling mantle and its incorporation into the oceanic crust occurred in the time-frame of a single melt input. Our cooling data are consistent with building of the oceanic crust at OCCs controlled by continuous uplift, in turn governed by long-lived detachment faults. The latter contribute to the rapid cooling of the assimilated mantle intervals and the magma bodies. Diffusion models of geochemical profiles in olivine from a single crustal section allow to reconstitute the early magmatic processes leading to mantle assimilation and early crystallization of gabbros, and the cooling history of the oceanic crust at OCC from magmatic conditions to hydrothermalism.

Research Data Related to this Submission

There are no linked research data sets for this submission. The following reason is given:
Data will be made available on request

Retrieving timescales of oceanic crustal evolution at Oceanic Core Complexes: Insights from diffusion modelling of geochemical profiles in olivine

Carlotta Ferrando[a,b,*], Kendra J. Lynn[c], Valentin Basch[d], Benoit Ildefonse[a] & Marguerite Godard[a]

Highlights:

- Diffusion modelling is powerful to unravel the history of oceanic crust formation.
- Mantle olivine composition can be completely reset in short minimum timescales.
- Mantle assimilation occurs in the time-frame of a single melt input every ~630 yr.
- Downhole cooling rates are constant from magmatic (1200°C) to low temperatures (250°C).
- Uplift contributes substantially to conductive cooling of the crustal sequence.

Retrieving timescales of oceanic crustal evolution at Oceanic Core Complexes: Insights from diffusion modelling of geochemical profiles in olivine

Carlotta Ferrando[a,b,*], Kendra J. Lynn[c], Valentin Basch[b], Benoit Ildefonse[a] & Marguerite Godard[a]

[a] Géosciences Montpellier, Université de Montpellier, CNRS, Université des Antilles, Montpellier, France

[b] Dipartimento di Scienze della Terra e dell'Ambiente, University of Pavia, Pavia, Italy

[c] Department of Earth Sciences, University of Delaware, Newark, DE 19713, USA

*Corresponding Author
Carlotta Ferrando

Email: ottaferrando@gmail.com

Abstract

The building of oceanic crust at Oceanic Core Complexes (OCC) has been described as a complex process involving multiple intrusions of magma over a protracted period of time. The migration of primitive magmas (i.e., Mid Ocean Ridge Basalts, MORBs) can lead to melt-rock interactions during reactive porous flow processes through the lithosphere. The timescales of these reactive processes and the subsequent cooling of the modified crystal matrix remain unconstrained. Diffusion modelling has been widely used to retrieve timescales of magmatic processes. In this study, we use diffusion models to constrain *(i)* the minimum timescales of melt-rock interactions and *(ii)* the cooling rates of the gabbroic sequence forming the oceanic crust at an OCC. We chose samples of the most primitive olivine-rich troctolites from the gabbroic sequence sampled in IODP Hole U1309D (Atlantis Massif OCC, Mid-Atlantic Ridge 30°N). Olivine-rich troctolites were interpreted as marking local partial assimilation of mantle intervals into the oceanic crust, and thus allowed to understand the dynamics of mantle assimilation and the formation of slow-spreading oceanic crust at the Atlantis Massif OCC. Olivines in olivine-rich troctolites represent relicts of pre-existing mantle olivine, while clinopyroxenes and plagioclases are crystallized during reactive percolation. Olivine chemical compositions show that olivine-rich troctolites inherit chemical heterogeneity from the mantle precursor. Flat geochemical profiles in olivine indicate complete chemical re-equilibration of olivine crystals with the locally modified percolating melt. Exception is made for most Ca profiles that show lower Ca contents at the olivine rim compared to the relative crystal core, as the result of subsolidus cooling. Three-dimensional (3D) diffusion models at magmatic conditions (T = 1210-1300°C and P = 2 kbar) reveal that complete chemical re-equilibration of 4 mm-size mantle-derived olivine with percolating MORB-type melts can be attained within durations of less than 300 yr. The Ca-in-olivine geospeedometer reveal that cooling rates from ~1200°C to ~1050°C are constant downhole and on average 0.004 °C/yr; they are comparable with lower temperature cooling rates (850°C-250°C) estimated at the Atlantis Massif OCC. The minimum timescales from 3D models point to rather fast re-equilibration of olivine. The downhole chemical heterogeneity inherited from the precursor mantle, coupled with the timescales of diffusive re-equilibration suggest that the partial assimilation of the

upwelling mantle and its incorporation into the oceanic crust occurred in the time-frame of a single melt input. Our cooling data are consistent with building of the oceanic crust at OCCs controlled by continuous uplift, in turn governed by long-lived detachment faults. The latter contribute to the rapid cooling of the assimilated mantle intervals and the magma bodies. Diffusion models of geochemical profiles in olivine from a single crustal section allow to reconstitute the early magmatic processes leading to mantle assimilation and early crystallization of gabbros, and the cooling history of the oceanic crust at OCC from magmatic conditions to hydrothermalism.

Keywords: lower oceanic crust at the Atlantis Massif; olivine trace elements; diffusive re-equilibration; oceanic crustal cooling; magma emplacement; exhumation by detachment faults

1. Introduction

Melts generated by adiabatic melting of the upwelling mantle beneath mid-ocean ridges are supplied to the magmatic plumbing system, where they undergo complex processes of magma crystallization, mixing and/or assimilation of a pre-existing crystal matrix prior to eruption on the seafloor (e.g., Brandl et al., 2016; Coogan and O'Hara, 2015; O'Hara, 1977; O'Neill and Jenner, 2012). These processes are recorded in the lower oceanic crust beneath oceanic spreading centers. Recent studies have demonstrated the importance of reactive porous flow and melt-rock interactions in the construction of the gabbroic lower crust, in particular along slow-spreading ridges (e.g., Dick et al., 2010; Drouin et al., 2009, 2010; Lissenberg and Dick, 2008; Lissenberg and MacLeod, 2016; Lissenberg et al., 2019; Sanfilippo et al., 2015) and in their ophiolite analogues (e.g., Basch et al., 2019a, 2019b, 2018; Bédard, 1993, 2001; Bédard and Hébert, 1996; Rampone et al., 2020; Sanfilippo et al., 2014). These reactive processes are thought to occur in cooling yet still partially molten magmatic systems, possibly at the transition between lithospheric mantle and the magmatic lower oceanic crust (e.g., Collier and Kelemen, 2010; Ferrando et al., 2018; Rampone et al., 2020; Sanfilippo et al., 2015). To better understand the mechanisms driving the formation of slow-spreading oceanic crust, it is imperative to constrain the timescales of the processes involved in its evolution from early magmatic differentiation of melts (i.e., crystallization and dissolution-precipitation reactions) to cooling of the crustal sequence (i.e., crystal-dominated system).

Timescales of magmatic emplacement beneath slow-spreading ridges have been determined for crustal sections exposed along the Mid-Atlantic Ridge (MAR; e.g., Grimes et al., 2008), while duration of cooling have been concurrently estimated by other authors for the lower oceanic crust beneath both the MAR and the Southwest Indian Ridge (SWIR) (e.g., Grimes et al., 2011; John et al., 2004; Schoolmeesters et al., 2012). John et al. (2004) documented the thermal structure of oceanic lithosphere beneath the ultraslow-spreading SWIR. They applied thermochronometric techniques on minerals in felsic veins (crystallization at ~850°C), thus lacking direct constraints on the earlier magma emplacement history at higher temperatures (from ~1250°C to ~850°C). A broad reconstruction of timescales of oceanic crustal evolution from high temperature magma emplacement

90 to cooling of the gabbroic sequence has not yet been established for a single suite of samples. In this
91 contribution, we use the geochemical composition of olivines from the widely investigated primitive
92 olivine-rich troctolites recovered at Atlantis Massif (IODP Hole U1309D; Blackman et al., 2006) to
93 provide timing of magmatic processes occurring at temperatures of about 1230°C and of cooling of the
94 lower oceanic crust down to about 1000°C.

95 Olivine-rich troctolites from the oceanic crustal section at the Atlantis Massif Oceanic Core
96 Complex (OCC; IODP Hole U1309D; Blackman et al., 2006) are one of the best studied olivine-rich
97 lithologies (i.e., with >70% modal olivine) worldwide. They were interpreted to result from partial
98 mantle assimilation during reactive porous flow of a MORB-type melt (Drouin et al., 2007, 2009,
99 2010; Suhr et al., 2008; Ferrando et al., 2018). Olivine-rich troctolites from Hole U1309D were
100 selected for this study because they are unique samples from active spreading ridges that record the
101 oceanic crustal evolution from early magmatic processes of melt-rock interaction and crystallization of
102 a primitive MORB, to exhumation and cooling during OCC formation. We apply diffusion modelling
103 to provide a comprehensive dataset of timescales related to these magmatic processes and to
104 reconstruct the geodynamic evolution of the oceanic crust from the Atlantis Massif OCC.

105 Diffusion modelling of chemical species in rock-forming minerals is a tool widely used to quantify
106 the timescales of magmatic processes such as magma assimilation (e.g., Bindeman et al., 2006; Costa
107 and Dungan, 2005), magma mixing (e.g., Chamberlain et al., 2014; Lynn et al., 2017a), magma
108 residence time before eruption (e.g., Lynn et al., 2018; Nakamura, 1995), and subsolidus cooling rates
109 of magmatic bodies (e.g., Coogan et al., 2007, 2002; Faak et al., 2013; Faak and Gillis, 2016; Sun and
110 Lissenberg, 2018). Many theoretical and experimental studies have investigated the crystallographic
111 and chemical parameters controlling diffusion of major, minor and trace elements in mafic minerals,
112 most particularly olivine, thus significantly improving the available diffusion coefficient database
113 (e.g., Coogan et al., 2005; Dohmen and Chakraborty, 2007; Petry et al., 2004; Spandler and O'Neill,
114 2010). Concurrently, progresses in analytical techniques now allow measurement *in situ* of a broad
115 range of chemical elements down to very low concentrations (<<ppm) such as Rare Earth Elements
116 (REE) in olivine (e.g., Basch et al., 2018; D'Errico et al., 2016; Drouin et al., 2009; Ferrando et al.,

2018; Rampone et al., 2016; Sanfilippo et al., 2014). These developments allow the collection of chemical profiles for many elements that have different rates of diffusion, thus permitting detailed investigations on the timescales of complex processes.

In this study, we used geochemical profiles (Ferrando et al., 2018 and this study) in olivine because it is the only phase present from the mantle protolith to the reactive formation and cooling of olivine-rich troctolites. Geochemical profiles record two processes: *(i)* flat profiles of olivine forsterite content (Fo) and Ni, Mn, Co and Zn compositions indicate complete re-equilibration of olivine with the percolating melt during melt-rock interactions; and *(ii)* convex profiles of Ca, Y and Yb document subsolidus re-equilibration during cooling. However, timescales of the high-temperature (hereafter referred to as 'magmatic temperatures') reactive process and cooling remain to be estimated.

(i) We reproduce the measured homogeneous element profiles by numerically modelling their chemical diffusive re-equilibration and retrieve minimum timescale estimates of high temperature (> 1200°C) re-equilibration. To account for diffusion anisotropy in olivine ($D_{[001]} > D_{[010]} \approx D_{[100]}$ for Fe-Mg, Ni and Mn, $D_{[001]} >> D_{[100]} > D_{[010]}$ for Co, while Ca, Y and Lu are nearly isotropic; Table 1 and references therein), and to consider the influence of spatial dimensions, crystal morphology, and sectioning, we used a three-dimensional (3D) numerical model (Jollands and Müntener, 2019; Lynn et al., 2017b; Shea et al. 2015). Simultaneous diffusive re-equilibration of eight diffusing species comprising major, minor and trace elements (Fe-Mg, Ni, Mn, Ca, Co, Zn, Y, Yb) in olivine were modelled. Our results provide the first constraints on the timing of melt-rock interactions largely described at oceanic spreading centers.

(ii) Subsolidus cooling rates have been previously investigated in the oceanic crust at the Atlantis Massif OCC, although most constraints document the latest stages of cooling (below 780°; Grimes et al., 2011; Schoolmeesters et al., 2012) and cooling rates in the temperature interval from magmatic conditions (~1200°C) down to 900-800°C remain unconstrained. In this study, calcium zoning in olivine is modelled using the Ca-in-olivine geospeedometer (Coogan et al., 2007, 2002) to determine ~1200°C to ~1000°C subsolidus cooling rates of Hole U1309D olivine-rich troctolites.

143 The results of this study characterize the timing of mantle incorporation into the oceanic crust,
144 which are used to reconstruct the thermal history and subsolidus cooling of the gabbroic sequence
145 formed at an OCC, from high magmatic temperatures down to ~250°C.

146

147 ## 2. Geological setting and sampling

148 ### *2.1 The oceanic crustal sequence at Atlantis Massif*

149 Atlantis Massif is a domal structure located at 30°N on the western flank of the slow-spreading
150 MAR, at the intersection with the Atlantis transform fault (Fig. 1a). The corrugated core of the dome is
151 a ~2 Ma old OCC where oceanic crust is exposed via a long-lived and low-angle detachment fault
152 (e.g., Blackman et al., 2002; Ildefonse et al., 2007).

153 On the central dome of Atlantis Massif, IODP Hole U1309D (Fig.1a) penetrated 1415.5 m below
154 seafloor (mbsf) through a complex gabbroic sequence (IODP Expedition 304/305; Blackman et al.,
155 2011). The recovered section is highly heterogeneous and comprises ~85% of gabbro, gabbronorite
156 and olivine gabbro, with lesser oxide gabbro (7%) and minor MORB-type diabase intrusions (3%).
157 The downhole lithostratigraphy is characterized by numerous inter-fingered intrusive bodies varying
158 in thickness, with more evolved lithologies generally intrusive into less evolved lithologies (e.g.,
159 Blackman et al., 2006). Bulk Mg-values (Mg# (cationic ratio) = $100\times Mg/(Mg+Fe_{total})$) vary from 60 to
160 90 mol%, with local exceptions of lower values characterizing the most evolved lithologies (Fig. 1c).
161 No systematic compositional trends are observed downhole (i.e., trend of fractional crystallization;
162 Godard et al., 2009). Such complex structural and textural relationships, together with chemical
163 evolution confined in discrete lenses and the variable downhole zircon ages indicate that melt
164 injections occurred at random depths during the construction of the gabbroic sequence (Blackman et
165 al., 2006; Godard et al., 2009; Grimes et al., 2008). The total duration of magmatic accretion was
166 inferred to be ~200 ka by radiometric dating of zircons (Grimes et al., 2008; Fig. 1c) and occurred
167 over two main periods, with an older intrusive event forming the deepest interval from 600 mbsf to the

bottom of the hole (~1.24 Ma average) and a younger event occurring throughout the core (~1.17 Ma average). Grimes et al. (2008) inferred that emplacement of the oldest and deepest 635 m-thick lower crustal interval in Hole U1309D occurred within ~150 kyrs at a continuous growth rate of 1.6 cm/yr. These estimations, together with the recognition of over 250 intrusive igneous contacts throughout the Hole, allowed assessing an average thickness of single magma sills of 10 m and their emplacement every 630 yrs (Grimes et al., 2008).

Minor discrete intervals of serpentinized and locally impregnated residual harzburgite (<1% of total recovery in Hole U1309D; Godard et al., 2009; Tamura et al., 2008) were identified within the first ~200m of Site U1309. Mantle rocks disappear downhole and ultramafic intervals are represented by olivine-rich troctolites (Ol-T; 70-90% olivine, 5-25% plagioclase, 5-25% clinopyroxene; Fig.1b) occurring in 22 discrete intervals and covering ~5% of total recovery (Blackman et al., 2006).

2.2 Hole U1309D olivine-rich troctolites

Ol-T is the dominant lithology in the interval between 1100 and 1300 mbsf (Fig. 1) and is locally very fresh with <1% serpentinization. Drouin et al. (2010, 2009) and Suhr et al. (2008) interpreted Ol-Ts from the Atlantis Massif OCC as resulting from melt-rock interaction in a reactive porous flow process. Ferrando et al. (2018) demonstrated that the multi-stage reactive process is triggered by melt infiltration into mantle harzburgite. Reactive percolation of MORB-type melts leads to mantle olivine dissolution, which locally modifies the composition of melts. In turn, the tholeiitic crystallization suite is modified: concomitant crystallization of interstitial clinopyroxene and plagioclase occurs whilst olivine is re-equilibrating with the migrating melt (Drouin et al., 2009; Ferrando et al., 2018). Ferrando et al. (2018) posit that, as temperature decreases, locally modified melts partially crystallize in cross-cutting gabbroic veins and finally form part of the gabbroic intrusions building the crustal sequence at the Atlantis Massif OCC.

At the grain scale, during the open-system process of mantle-melt interaction, olivine is eroded (i.e., partial dissolution) and partially precipitated at crystal rims (Ferrando et al., 2018). The large

194 variations and non-systematic downhole correlations of Ni and Li contents (Ni = 1800-2820 ppm; Li =
195 1.5–2.9 ppm) in olivine from Ol-Ts (Fig. 1d) are locally inherited from the precursor heterogeneous
196 mantle (Fig. 10 in Ferrando et al., 2018). Ferrando et al. (2018) defined two endmember Ol-Ts on the
197 basis of their structural and textural characteristics, and of their olivine composition. Ol-T1 (<77 vol%
198 modal olivine; Table 2) is the most reacted end-member (i.e. more mantle olivine dissolution)
199 characterized by olivine grains showing Mg# ~85 mol% and Ni contents between 1870 and 2820
200 ppm, embedded in large oikocrysts of plagioclase and clinopyroxene (Fig. 4e in Ferrando et al., 2018).
201 Ol-T2 (>77 vol% modal olivine; Table 2) is the least reacted end-member with olivine displaying
202 more evolved composition compared with Ol-T1 (Mg# ~84 mol% and Ni = 1790–2130 ppm) and
203 forming aggregates with interstitial plagioclase and minor clinopyroxene (Fig. 4f in Ferrando et al.,
204 2018). In both Ol-T1 and Ol-T2 olivine compositions are in equilibrium with adjacent clinopyroxene
205 and plagioclase (Fig. 8-9 in Ferrando et al., 2018).

206 Geochemical profiles in olivine (Fig. 2, Supplementary Material Fig. S1a,b) were performed by
207 Ferrando et al. (2018) and in this study along preferred crystallographic directions that were
208 determined by Electron Backscatter Diffraction analyses (EBSD). These profiles record two distinct
209 processes that involved chemical diffusive re-equilibration, first at magmatic temperatures (~1250°C)
210 during melt-rock interactions and subsequently at decreasing temperature under subsolidus conditions
211 (down to ~1000°C) during cooling.

212 At magmatic temperatures, the fast diffusive transport of elements in olivine (e.g., Dohmen and
213 Chakraborty, 2007), which overall shows less than three orders of magnitude difference in diffusivity
214 (Table 1), is able to reset olivine compositions. Consistently, Fo [Fo = 100×Mg/(Mg+Fe)], Ni, Mn, Co
215 and Zn show flat profiles in all principal crystallographic directions ([100], [010] and [001];
216 Supplementary Material Fig. S1a,b). Flat profiles in olivine are interpreted to be the result of complete
217 diffusive re-equilibration with the reacted and modified percolating melt during melt-rock interactions.
218 These profiles can be used to quantify the minimum timescales over which chemical re-equilibration
219 likely occurred. This process of olivine re-equilibration is herein referred to as 'diffusive re-
220 equilibration at magmatic temperatures (MT diffusive re-equilibration)'.

Although Ca in olivine was likely also completely re-equilibrated during melt-rock interactions, Ca profiles show lower Ca contents at the olivine crystal rim compared to the relative crystal core (Fig. 2). Similar convex profiles are documented in some olivine crystals also for Y and Heavy- REE (HREE, e.g., Yb; Fig. 2 and Supplementary Material Fig. S1a,b). Being preferentially hosted in clinopyroxene, Ca, Y and HREE can diffuse from olivine into clinopyroxene at subsolidus conditions due to the dependence of element partitioning on temperature decrease (e.g., Coogan et al., 2002; Witt-Eickschen and O'Neill, 2005). In turn, the rate of diffusion decreases at decreasing temperature (e.g. Coogan et al., 2005) hampering complete re-equilibration of olivine core with the relative olivine rim at subsolidus conditions. We thus infer that convex profiles do not result from the previous complete MT diffusive re-equilibration during melt-rock interactions (i.e., leading to flat profiles). They rather record subsolidus cooling after magma emplacement (see discussion below).

3. Methodology

3.1. Geochemical profiles in olivine

The mineral modal contents, textures (grain size and phase relationships) and microstructures analysed by EBSD are described in Ferrando et al. (2018). We focused this study on core-rim geochemical variations in 42 olivine grains from samples of Ol-T1 and Ol-T2, and we report complementary analyses of *in situ* major and trace element compositions (Fig. 2 and Supplementary Material Table S1). A subset of 12 most representative rim-core-rim profiles is shown in Supplementary Material Figures S1a and S1b. Absolute concentrations of Yb are the highest of the Rare Earth Elements (REE) in olivine (Supplementary Material Table S1), therefore we report Yb in Figure 2 as representative of olivine REE concentrations.

Because element diffusion is overall anisotropic, geochemical profiles were collected along preferred directions selected parallel to (at least) one of the three principal crystallographic axis of olivine having axes plunge (measured from the sample surface) <5° (Ferrando et al., 2018). All three crystallographic directions of olivine were investigated in each sample. Core-rim and rim-to-rim

247 traverses were measured with 19-80 µm spacing for major and minor elements, and 70-500 µm for
248 trace elements (Supplementary Material Table S1).

249 Major elements and trace elements were determined using analytical instruments from the
250 Microsonde Sud (Géosciences Montpellier, University of Montpellier). Major elements were
251 measured by Electron Probe Micro Analyser (EPMA) using a CAMECA SX100 equipped with five
252 wavelength-dispersive X-ray spectrometers (WDS); accelerating potential was set to 20 kV, beam
253 current at 10 nA, and counting times were 30 s for all elements. Natural minerals and synthetic oxides
254 are used as standards. *In situ* trace elements were measured after EPMA analyses to minimize loss of
255 sample. Surface cleaning was performed on the selected EPMA spot by pre-ablation in 5-6 pulse per
256 second. We used a Thermo Scientific Element 2 XR (eXtended Range) high resolution - Inductively
257 Coupled Plasma Mass Spectrometry (ICPMS). The ICP-MS is coupled with laser ablation (LA)
258 system, a Microlas (Geolas Q+) automated platform with a 193 nm Excimer Compex 102 laser from
259 LambdaPhysik. An in-house modified 30 cm^3 ablation cell with a helium atmosphere was used to
260 enhance sensitivity and reduce inter-element fractionation (Günther and Heinrich, 1999). The laser
261 energy density was set to 12–15 J cm^2 and repetition rate at 8–10 Hz. The laser spot size was 102–77
262 µm. Data were collected in time resolved acquisition mode with the background signal collected for 2
263 min followed by 1 min of sample ablation, or with 2.33 min for the blank and 40 s sampling.
264 Concentrations were calibrated against the NIST 612 rhyolitic glass using the values given in Pearce et
265 al. (1997). Data were reduced with the GLITTER software package (Van Achterbergh et al., 2001)
266 using the linear fit to ratio method, and ^{29}Si was used for internal standardization relative to EPMA
267 data. Signals were carefully monitored and data were filtered for spikes on an element by element
268 basis. Detection limits were between 0.07 and 1 ppm for Ni, <55 ppb for Mn, Cu, Zn and <22 ppb for
269 Co; they were <5 ppb for most incompatible elements (i.e., Y and HREE). Reference basalt BIR-1G
270 was used as internal standard to monitor accuracy as well as reproducibility within single series and
271 between runs. This resulted in reproducibility better than 5% for Co and REE, and it is <12% for all
272 other elements (see Ferrando et al. 2018 for details and Tables).

273

3.2. Numerical diffusion modelling

Diffusion in solids is described using Fick's law ($J_i = -D_i \partial C_i / \partial x$), which states that the concentration evolution of a chemical species i with time (flux J_i) is governed by its rate of diffusion (diffusion coefficient, D_i, m^2/s) and depends on the concentration gradient of i along a given direction x ($\partial C_i / \partial x$), where C_i is the concentration of i. Most numerical diffusion models are solutions of the Fick's second law (Crank, 1975). Several solutions of this equation have been published in the literature to evaluate the timescales of diffusion in minerals in various although simplified magmatic systems.

Flat profiles of Fo, Ni, Mn, Co and Zn were modelled to quantify the minimum timescales of MT diffusive re-equilibration (Fig. 2, Supplementary Material Fig. S1a,b). To account for diffusion anisotropy in olivine, and to consider the influence of crystal size, morphology, and sectioning, MT diffusive re-equilibration was simulated using three-dimensional (3D) diffusion models modified after Shea et al. (2015). Additionally, cooling rates were estimated using one-dimensional models (Ca-in-olivine geospeedometry; Dodson, 1973; Coogan et al., 2002, 2007) to fit CaO convex profiles measured in olivine (Fig. 2, Supplementary Material Fig. S1a,b). The choice of using a 1D model for Ca diffusion at subsolidus conditions is supported by the negligible dependence of Ca diffusion rates on the crystallographic orientation of olivine (Coogan et al., 2005); the CaO profiles are convex in most olivine crystals and in all measured directions, thus indicating that crystal shape and diffusion anisotropy (3D effects) did not affect Ca diffusion at subsolidus conditions. Among CaO convex profiles, those displaying flat plateaus at the crystal core were preferentially selected for models of Ca-in-olivine geospeedometry in this study. We avoided asymmetric CaO convex profiles and those showing dipping plateau, as they are common in sections that are off centre and/or oblique to principal crystallographic axes and can contribute to the uncertainty in retrieved cooling rates (e.g., Shea et al., 2015).

298 Data in this study are from olivines that span the range of observed grain sizes from 1 to 4 mm. In
299 the following sections we illustrate the details of MT diffusive re-equilibration models and Ca-in-
300 olivine geospeedometry.

301

302 *3.2.1 MT diffusive re-equilibration models*

303 Chemical re-equilibration in olivine was simulated for eight elements that were chosen on the basis
304 of their compatibility in olivine, from compatible (Fe-Mg [Fo], Ni) to moderately incompatible (Mn,
305 Co, Zn, Ca) and highly incompatible elements (Y, Lu). Trace elements were investigated as common
306 tracers of melt-rock interaction processes, during which their concentrations are strongly modified
307 (e.g., Basch et al., 2018; Ferrando et al., 2018; Rampone et al., 2016; Sanfilippo et al., 2014).
308 Moreover, the modelled elements cover a wide range of diffusion rates in olivine (Table 1) allowing
309 characterization of a broad range of minimum re-equilibration timescales.

310 Simulations were performed using three solutions of the 3D form of Fick's second law (Crank,
311 1975). Solutions for anisotropic diffusing species were applied for Fe-Mg, Ni, and Mn using the
312 concentration-dependent equation (Eq. A1), and Ca using the non-concentration dependent form (Eq.
313 A2); trace elements were modeled using the non-concentration dependent form for isotropic diffusion
314 (Eq. A3) (see Appendix A for details on the equations). Because anisotropic diffusion of Co was
315 documented exclusively at a single temperature condition (i.e., 1300°C; Spandler and O'Neill, 2010)
316 and the Arrhenius relationship for D_{Co} is only available for Co diffusion along the crystallographic
317 axis [001] ($D_{Co[001]}$, i.e., fast direction; Ito et al., 1999), we modelled isotropic diffusion of Co using
318 $D_{Co[001]}$ in Eq. A3. We are aware that this simplified approach possibly underestimates the timescales
319 computed from Co profiles (i.e., use of the fastest D_{Co}), but we emphasize that the overall D_{Co} is
320 comparable to the D_i of the other trace elements (see Table 1) thus leading to timescales in the same
321 order of magnitude as Y and REE.

322 Although simple crystal geometries and analytical solutions are often used to calculate timescales
323 of element diffusion, Shea et al. (2015) demonstrate that using spherical crystals lead to systematic

overestimations of timescales. Following these findings, olivine is here modelled with polyhedral morphology (Shea et al., 2015) allowing to reproduce a realistic olivine shape (Fig. 3). The best preserved olivine crystals in the studied Ol-Ts have dimensions typical of euhedral olivine crystals with *c*-axis >> *b*-axis > *a*-axis and *c*-axis ≈ 2 * *a*-axis (Supplementary Material Fig. S2). Comparable olivine crystal shapes have been previously documented by Welsch et al. (2014) in samples from the same Hole U1309D. Therefore, we assumed a euhedral crystal similar to olivines often described in erupted lavas (e.g., Lynn et al., 2017). The 3D olivine + melt models have dimensions of 221x221x221 voxels (a voxel being a pixel in three dimensions). The modelled olivine had dimensions of 201 voxels along the *c*-axis, 121 voxels along the *b*-axis, and 95 voxels along the *a*-axis (e.g., Shea et al., 2015; Fig. 3). Two crystal sizes reflecting the minimum and maximum olivine sizes observed in the thin sections were modelled with different voxel resolutions. For small grains *c*-axis was set ~1 mm long (resolution of 4x4x4 µm per voxel; olivine crystal of dimensions x=804 µm, y=484 µm, z=380 µm) and for coarser grains ~4 mm long (resolution of 20x20x20 µm per voxel; olivine crystal of dimensions x=4020 µm, y=2420 µm, z=1900 µm).

The advantage of the 3D model approach is that mineral core compositions can be tracked through time. This provides insights into how resilient original mantle olivine compositions are to being overprinted by secondary processes such as melt-rock interactions. A simplified estimate of diffusion distance using $x = \sqrt{(D_i t)}$ has been applied by numerous previous studies to infer the time (t) required to generate a diffusion profile of a given length (x) for an element of interest with known D_i. However, crystals are 3D objects subject to diffusive fluxes in all dimensions. While this simplified 1D equation might broadly characterize the time required for diffusive re-equilibration to reach a crystal's core, our 3D models allow us to determine how long it will take to completely re-equilibrate that core composition. Thus, this modeling approach is essential to understand how quickly minerals re-equilibrate with their surroundings and cannot be estimated using the simplified 1D equation.

The continuous change of melt composition at the interface between crystal and melt during dissolution-precipitation processes would be best modelled using moving compositional boundary conditions (e.g., Chakraborty, 2008) combined with changes in crystal shape (Chakraborty, 2018).

351 However, experimental investigations of reactive percolation of a primitive melt (MORB-type melt)
352 through a dunitic (Borghini et al., 2018) or troctolitic matrix (e.g.,Yang et al., 2019) documented that
353 at magmatic conditions (T~1250°C; similar to U1309D Ol-Ts formations) dissolution-reprecipitation
354 reactions of olivine are rapid, while Liang (2003) in an experimental and theoretical study of the
355 kinetics of melt-rock reaction demonstrated that diffusion of multiple elements in basaltic melts (of the
356 order ~10^{-11} m^2/s; e.g., Kress and Ghiorso, 1995; Liang, 2003) is faster than diffusive re-equilibration
357 in minerals (see Table 1). Also, we have no constraints on (*i*) the variation of melt volume due to
358 dissolution-precipitation, (*ii*) the composition of olivine and melt at a given stage of the reactive
359 process, and *(iii)* the effect of changes in crystal shape on diffusion rates. Therefore, for simplicity, we
360 modelled MT diffusive re-equilibration assuming static crystal shape and static boundary conditions
361 (e.g., constant melt composition). This assumption implies instantaneous change in melt composition
362 (i.e., fast element diffusion in melt; e.g., Liang, 2003) produced by melt-rock interactions and melt-
363 olivine equilibrium at the crystal rim.

364 Diffusion simulations were run until complete re-equilibration with the boundary condition was
365 achieved. 20 models were saved at equal intervals throughout the diffusion simulation to track the
366 evolution of the crystal's composition with time. These models were then sectioned through the
367 olivine crystal's core perpendicular to the *c*-axis (Fig. 3). The composition of the central pixel in the
368 2D section (Fig. 3) was sampled at regular intervals throughout the model diffusion time to track the
369 core compositional evolution. We also sampled 1D numerical traverses parallel to the *a*-axis in the
370 ideal 2D section to illustrate the evolution of compositional profiles with time. The extent of MT
371 diffusion is expressed in terms of % re-equilibration (noted % req; see Lynn et al., 2017b), which
372 allows a direct comparison among diffusing chemical species with different absolute concentrations
373 (e.g., ppm, wt%, mol%; Fig. 4a,c):

374 $$\%\ \mathrm{req} = \frac{(C_{initial} - C_{measured})}{(C_{initial} - C_{equilibrium})} \times 100 \qquad (1)$$

where $C_{initial}$ is the composition of mantle olivine before the onset of diffusion, $C_{measured}$ is the composition of the olivine core after a given time (expressed in years, examples in Fig. 4b), and $C_{equilibrium}$ is the composition of olivine in chemical equilibrium with the surrounding melt.

The magnitude of zoning in a 1D traverse parallel to the *a*-axis across olivine diminishes as time elapses and the profile becomes difficult to resolve analytically; distinctive inter-element zoning becomes less likely and the crystal nears "complete re-equilibration" beyond the kinetic window. We introduce the "effective % req" to take into account typical analytical uncertainties on each element (i.e., σ_i = average analytical error of the modelled element *i*). The effective % req adjusts the reported timescales with the analytical profiles that could realistically be resolved in natural samples as they near 100% equilibrium with the boundary conditions. Using the effective % req, we consider complete re-equilibration when olivine core composition in the 3D model reaches $C_{equilibrium} + \sigma_i$ (Table 3).

We ran the MT diffusive re-equilibration models at pressure of 2 kbar and oxygen fugacity at QFM (for Fe-Mg, Ni, Mn, and Ca), which are appropriate for the Atlantis Massif based on the estimated depths at which the gabbroic sequence was formed (~7 km; Grimes et al., 2008). Temperatures were set at 1230°C for models of Fo, Ni, Co, Mn, Ca (Fig. 4a), which correspond to the calculated crystallization temperature of plagioclase (Drouin et al., 2009). For the listed major and minor elements, models were also ran at 1210°C and 1250°C to account for uncertainties in the calculated timescales related to the +/- 23°C uncertainty of temperature estimate from Drouin et al. (2009). From these models at three different temperatures we calculated Δt_T, which is the uncertainty in modeled timescale related to the uncertainty in the temperature estimates. The uncertainty at the high end of the T range ($+\Delta t_T$) is the timescale at 1210°C – timescale at 1230°C, and the low end of the T range ($-\Delta t_T$) is the timescale at 1250°C – timescale at 1230°C. As no temperature-dependent equation is available for calculating D_{Zn}, D_{Lu} and D_Y (single value at 1300°C, Spandler and O'Neill, 2010; Table B1 in Appendix B), we also ran MT diffusive re-equilibration models of all elements at 1300°C and fO_2 = $10^{-8.3}$ bars (QFM-1; corresponding to the conditions of experiments in Spandler and O'Neill, 2010; Fig. 4c).

401

402 *Diffusion coefficients*

403 For the MT diffusive re-equilibration models, D_i were calculated at appropriate magmatic
404 temperatures, pressure and oxygen fugacity conditions using the Arrhenius relationships reported in
405 Table B1. Uncertainties in D_i are related to uncertainties in activation energies (~10%; e.g., Costa et
406 al., 2008), in turn leading to uncertainties in computed timescales of diffusion. D*i* calculated at
407 temperatures higher or lower than the temperature at which D_i was experimentally constrained can
408 have uncertainties of up to 3-4 orders of magnitude. In this study, D_i were calculated at temperatures
409 comprised in the temperature interval at which their Arrhenius relationships were experimentally
410 calibrated. This minimizes the uncertainties in timescales, which are likely encompassed by Δt_T and
411 uncertainties for olivine initial composition (see later in this section). Also, greater uncertainties in
412 timescales in these natural rocks are related to the variable grain size of olivine crystals that are here
413 treated modelling different crystal sizes.

414 To account for Fo variations, $D_{Fe\text{-}Mg(Fo)}$ and D_{Mn} were calculated using the diffusion coefficient
415 equations from Dohmen and Chakraborty (2007), and D_{Ni} from Petry et al. (2004) (Table B1). As no
416 such concentration-dependent equations are available for the Ca and Co, we calculated D_{Ca} and D_{Co}
417 using the Arrhenius relationships (Coogan et al., 2005 for Ca and Ito et al., 1999 for Co; Table B1)
418 calibrated for olivine Fo ~90.

419 Diffusion of REE is currently matter of debate and vast discrepancies exist between trace element
420 diffusivities in olivine with rates that span over several orders of magnitude (10^{-19}-10^{-20} m^2/s by
421 Cherniak, 2010; ~10^{-15} m^2/s by Spandler and O'Neill, 2010). This range may be related to the different
422 melt-powder compositions used in the experiments and, specifically, on the activity of SiO_2 and Ti
423 contents in the melt (Supplementary Material Fig. S3; see discussions in Jollands et al., 2016 and
424 Burgess and Cooper, 2013). The source of diffusant used by Spandler and O'Neill (2010) is a trace-
425 element-doped MORB-type melt containing 12 wt% of Al_2O_3 and 5 wt% of TiO_2, in contrast to the
426 synthesized mixture of REE (La, Dy, or Yb) aluminate and synthetic forsterite powders used by

Cherniak (2010) that does not reproduce a silicate melt (TiO_2 = 0 wt%). On the other hand, the experiments of Spandler and O'Neill (2010) (*i*) also use a San Carlos olivine with doped trace elements at levels that do not reflect natural olivine similarly to Cherniak (2010), and (*ii*) were conducted only at single temperature, pressure and oxygen fugacity conditions, which prohibit the extrapolation to temperatures other than 1300°C. Moreover, REE diffusion rates have been suggested to also depend on the mechanism of diffusion and concentration of diffusing species in olivine (Chakraborty, 2018). Similar to findings of Li diffusion (Dohmen et al., 2010), in most natural systems REE may diffuse via two mechanisms that differ in diffusion rate (Chakraborty, 2018); though, dependence of the active diffusion mechanism on the concentration of the diffusing species has never been defined, nor diffusion coefficients for these different mechanisms have ever been quantified.

Because only the experiments of Spandler and O'Neill (2010) include the buffering of all chemical activities (e.g., $aSiO_2$) and because the computed melt composition in equilibrium with interstitial clinopyroxene (see Ferrando et al., 2018) contains ~12-14 wt% of Al_2O_3 we posit that the $D_{REE,Y}$ (for D_{REE} only D_{Lu} is available) values from Spandler and O'Neill (2010) are the most appropriate for modelling minimum timescales of re-equilibration after melt-rock reactions at Atlantis Massif. For this reason, we selected D_{Zn}, D_{Lu} and D_Y single values from Spandler and O'Neill (2010). The use of fast diffusivities may lead to underestimation of timescales, and our model results represent minimum timescales of re-equilibration.

Initial and boundary conditions

Following the outcome of previous studies (see *Section 2.2*) on the reactive origin of Ol-Ts from assimilated mantle, we assumed that the initial composition of olivine is that of olivines in mantle harzburgites ($C_{initial}$ in Eq. 1). Mantle harzburgites sampled at modern ridges are compositionally heterogeneous due to different extents of mantle melting and impregnation processes (e.g., D'Errico et al., 2016; Regelous et al., 2016; Tamura et al., 2008). Also, among the little data available of *in situ* trace element composition of olivines in abyssal harzburgite (e.g., D'Errico et al., 2016; Regelous et

al., 2016) none is from samples collected at the Atlantis Massif OCC. The Gakkel Ridge is a slow- to ultra-slow avolcanic spreading ridge, similar to the region of MAR where the Atlantis Massif OCC is located. For these reasons, we explored the variation in timescales of MT diffusive re-equilibration using two different initial compositions (Table B2): *(i)* C_0a is the average composition of olivine in harzburgites from Gakkel Ridge (D'Errico et al., 2016; Regelous et al., 2016); *(ii)* C_0b is the composition of a single harzburgite olivine corresponding to that used by Ferrando et al. (2018) (values of Zn and Co are averages of the most primitive olivines from the global database of abyssal peridotite compositions in Regelous et al., 2016). The resulting variation in modeled timescale related to initial compositions is expressed as $\Delta t_x = |t(C_0a) - t(C_0b)|$, where $t(C_0a)$ and $t(C_0b)$ are timescales calculated for C_0a and C_0b, respectively.

Boundary conditions for the models are set to the measured olivine compositions, which represent the last reacted melt composition that is in equilibrium with adjacent clinopyroxene and plagioclase present in Ol-T ($C_{equilibrium}$ in Eq. 1). Boundary melt compositions are constrained by the averages of olivine composition in the U1309D Ol-T1 (Ferrando et al., 2018; summarized in Table B2), as representative of the most reacted Ol-Ts.

3.2.2 Ca-in-olivine cooling speedometry

After all melt has crystallized, the temperature dependence of partition coefficients (K_d) between minerals (e.g., Coogan et al., 2002; Witt-Eickschen and O'Neill, 2005) controls the re-distribution of elements during subsolidus cooling at the rims of adjacent phases, and a core-rim compositional gradient is produced within single crystals. The down-temperature dependence of Ca, Y and REE partitioning between olivine and clinopyroxene leads to the re-distribution of these elements from olivine rims to adjacent clinopyroxenes. Diffusion rates in olivine also decrease with decreasing temperature (e.g., Coogan et al., 2002; Dohmen and Chakraborty, 2007), resulting in incomplete chemical re-equilibration of the crystal, in turn generating core-to-rim variations in slow-diffusing elements, such as Ca content. Calcium is often used to retrieve timescales of subsolidus cooling (e.g.,

Coogan et al., 2007; Faak and Gillis, 2016). In this study, we determine the cooling rates and closure temperatures for 7 selected olivine grains that record a progressive decrease of Ca, Y and REE contents toward the crystal rim, applying the Ca-in-olivine geospeedometry (Eq. A4 in Appendix A) following the methods of Coogan et al. (2007). Here, the term 'closure temperature' describes the low temperature at which no appreciable Ca diffusion occurs in the studied olivine (measured using the geothermometer by Köhler and Brey, 1990; see Coogan et al., 2007). We used the D_{Ca} from Coogan et al. (2005) (Eq. A5 in Appendix A) as it is consistent with the most recent measurements by Bloch et al. (2019), who combined LA-ICP-MS, SIMS and atom probe (LEAP) analytical techniques. The Ca-in-olivine method assumes clinopyroxene is an infinite reservoir for Ca, thus we selected only olivines in contact with clinopyroxene.

Because clinopyroxene has much higher Ca, Y and REE contents (here on average, CaO = 21 wt%) compared to those of olivine (here on average, CaO = 0.08 wt%), no core-to-rim variations are generally observed in clinopyroxene (i.e., infinite reservoir boundary condition).

Initial conditions for the diffusion model were homogeneous and set to the Ca content measured in the core of the olivine crystal (Fig. 5 and Supplementary Material Fig. S4). Initial model temperatures were determined using the partition coefficient for Ca between olivine and clinopyroxene (Köhler and Brey, 1990) and the Ca content preserved in the olivine core plateau. This initial temperature was then used to calculate the initial D_{Ca} used in the diffusion model (D_{Ca} from Eq. A5 in Appendix A). After one model iteration, the time elapsed (∂t) was used to determine the change in temperature (ΔT) as a function of an assumed cooling rate. We recalculated the partition coefficient, temperature, and diffusion coefficient for Ca after each time-step throughout the models to extract linear cooling rates; different cooling rates were imposed on the models until a best fit to the measured profile was obtained (Fig. 5 and Supplementary Material Fig. S4). The total time elapsed represents only the diffusion time recorded by the zoning generated between the initial and closure temperatures. Thus, they are minimum estimates of the duration of high-T cooling histories.

505 ## 4. Results

506 ### *4.1 Timescales of mantle assimilation into the crust*

507 Timescales of diffusive re-equilibration after mantle-melt interactions are reported in Table 3 and
508 in Figure 4 at given % req. Because there is no chemical zoning in olivine (except Ca; Fig. 2 and
509 Supplementary Material Fig. S1a,b), we have no constraints on the time elapsed after complete re-
510 equilibration (past the kinetic window) and therefore, the determined timescales are first order
511 minimum durations. Timescales can change as a function of temperature, initial conditions and grain
512 size. The related variability of MT diffusive re-equilibration timescales is reported in the following.

513 The 1230°C 3D modelling of 4 mm olivine grains using C_0a as starting olivine composition show
514 complete MT diffusive re-equilibration (i.e., effective ~100% req) within 220 years for all major and
515 minor elements (Fe-Mg, Ni, Mn, Co, Ca; Table 3 and Fig. 4a). Using C_0b as starting composition for
516 the same set temperature and grain size provides timescales lower than 250 yr, leading to $\Delta t_X < 100$ yr
517 (Table 3). Models ran at 1210°C and 1250°C allowed us to test the variability in timescales related to
518 the uncertainty of the geothermometric estimates (T = 1230 +/- 23°C). The 1210°C models yield the
519 highest values of minimum durations of diffusive re-equilibration among all models. The variability in
520 timescales (Δt_T) between models at 1230°C (taken as reference values) and at 1210°C and 1250°C
521 ranges from +/- 5 yr to +/-40 yr between all investigated elements (Table 3). At any given T, initial
522 composition and % req, the time of re-equilibration of an element decreases with decreasing grain size
523 (from 4 mm to 1 mm in Fig. 4a,c), as equilibrium can be achieved more rapidly in smaller crystals.

524 The models of MT diffusive re-equilibration at 1300°C allow comparison between all investigated
525 elements including Zn, Y and Lu (see *3.1 MT diffusive re-equilibration models*). They yield shorter
526 timescales compared to those simulated at 1230°C (Fig. 4) due to the T-dependence of D_i (faster
527 diffusivities at higher T). For olivine grains of 4 mm size and C_0a as starting olivine composition, the
528 1300°C 3D models show that Zn displays the shortest re-equilibration time of ~14 yr, followed by Co
529 (28 yr), Y (40 yr), Lu (44 yr), Ni (84 yr), Ca (117 yr), Fe-Mg and Mn (120-125 yr) (Table 3 and Fig.
530 4c). The construction of 2D sections (Fig. 3) also permits sampling of 1D rim-core-rim profiles across

531 the olivine models. With these data we can track the evolution of the composition of olivine zoning
532 patterns at regular intervals throughout the 1 mm 3D models at 1230°C for representative major
533 elements (Fo), and compatible (Ni) and moderately incompatible (Mn) minor elements (Fig. 4b).
534 Elements are re-equilibrated at relatively constant rate up to 80% req (Fig. 4) of the olivine core. Fo
535 content decreases and Ni and Mn increase until 80% relative to the starting composition (C_0a) within
536 15 years (Fig. 4b). To attain complete re-equilibration other ~10 years are necessary, showing that the
537 re-equilibration process progressively slows down as crystal nears complete re-equilibration (last
538 ~20% req.), due to decreasing compositional gradient (Fig. 4).

539 Regardless of the grain size, set temperature and initial composition, all elements spanning from
540 Fe-Mg to incompatible REE (i. e., Lu) and Y show complete re-equilibration in olivine within 300
541 years (Table 3 and Fig. 4). We recall that in MT diffusive re-equilibration models from this study we
542 assumed a polyhedral morphology of olivine (i.e., euhedral crystal). On the other hand, models of
543 crystals with more equant aspect ratios, and thus ultimately a smaller volume, would result in even
544 shorter re-equilibration timescales (e.g., Shea et al., 2015).

545 Overall, the computed minimum durations of re-equilibration are lower than the 630 yrs (light grey
546 band in Fig. 4) estimated for the frequency of emplacement of 10 m-thick sills, and overall lower than
547 the total ~150 kyrs emplacement of the oldest and deepest 635 m-thick lower crustal interval (from
548 600 to 1235 mbsf) in the Atlantis Massif OCC (Grimes et al., 2008).

549

550 *4.2. Timescales of subsolidus re-equilibration*

551 Ca, Y and REE are preferentially hosted in clinopyroxene. Ca contents (in wt% from EPMA
552 analyses) are systematically lower at olivine rim compared to the crystal core (Fig. 2 and
553 Supplementary Material Table S1 and Fig. S1a,b). Y and Yb concentrations (in ppm from LA-ICP-MS
554 analyses) are either constant in single olivines, or slightly lower at the crystal rim in comparison with
555 the corresponding core (Fig. 2 and Supplementary Material Table S1 and Fig. S1a,b). Nonetheless,
556 because of serpentinization along olivine edges, most geochemical analyses were performed at a

minimum distance of 50 µm from olivine grain boundary leading to a gap in data at the actual mineral/mineral interface. Moreover, the low concentration of trace elements in olivine force setting large spot sizes (102-77 µm in this study), which possibly prevent the analyses of compositional variations at the rim of the olivine crystal. As a consequence, we cannot preclude possible local chemical variations at olivine rims for some elements, which can explain the flat Y and Yb profiles measured in most discarded olivine grains and some selected olivines (Supplementary Material Fig. S1a,b).

Core-to-rim chemical variations in olivine suggest that Ca, and to a lesser extent Y and Yb, diffused from olivine into the adjacent phases (i.e., plagioclase and clinopyroxene), as the effect of subsolidus diffusive re-equilibration driven by a temperature sensitive K_d during cooling of the gabbroic sequence at the Atlantis Massif.

Partitioning of other elements, such as Mg-Fe and Ni, is also temperature-sensitive (e.g., Faak et al., 2013; Roeder and Emslie, 1970; Witt-Eickschen and O'Neill, 2005). Olivine acts as an infinite reservoir for compatible elements, nominally Ni and Mg, at decreasing temperature similarly to Ca in clinopyroxene. Cooling of gabbroic rocks can induce chemical re-distribution of Ni and Mg into olivine from clinopyroxene and plagioclase, respectively (Faak et al., 2013; Witt-Eickschen and O'Neill, 2005). If this was the case for olivines in Hole U1309D Ol-Ts, diffusion of Ni and Mg# from clinopyroxene and plagioclase into olivine would have resulted in convex profiles of Mg# in plagioclase (e.g., Faak et al., 2013; Sun and Lissenberg, 2018) and Ni in clinopyroxene during cooling. However, no zoning of Mg# or Ni contents is observed in clinopyroxene and plagioclase (Supplementary Material Fig. S5). Because element diffusion in clinopyroxene and plagioclase is slower than diffusion in olivine (D_{Cpx} ~10^{-19}-10^{-21}; e.g., Van Orman et al., 2001; Zhang et al., 2010; D_{MgPlag} = ~10^{-16}; Faak et al., 2013), Ni and Mg# contents decrease at the very edge of plagioclase and clinopyroxene crystals without further concentration change (i.e., lack of element diffusion) toward the crystal cores. Such concentration variations (likely at the order of few µm) cannot be detected at the resolution of the laser spot size (77 µm), and therefore it is plausible that subsolidus re-equilibration of plagioclase and clinopyroxene was simply not detected in the studied Ol-Ts. On the olivine side, Mg#

584 and Ni contents would increase of just a negligible amount because they are substantially more
585 concentrated in olivine than in the adjacent phases (i.e., olivine infinite reservoir). At the resolution of
586 EPMA and LA-ICP-MS used in this study, these chemical variations are also not detectable.
587 Moreover, olivine, clinopyroxene and plagioclase should record equilibrium temperatures close to
588 1000°C if compositions were modified at subsolidus conditions (e.g., Coogan et al., 2002; Sun and
589 Liang, 2014). Mineral chemical compositions indicate that these phases in Hole U1309D Ol-Ts are in
590 equilibrium at temperatures between 1190°C and 1205°C with a melt showing Mg# = 58-65 mol%
591 (Ferrando et al., 2018). The high equilibrium temperatures, together with the (apparent) lack of Ni and
592 Mg zoning and olivine acting as infinite reservoir, indicate that flat profiles of elements preferentially
593 hosted in olivine record magmatic processes, and that those concentrations in the studied olivine were
594 likely not modified, or increased to a negligible extent, during cooling.

595 Initial temperatures recorded by olivine core Ca contents are on average ~1200°C. Closure
596 temperatures recorded by olivine rims range between 1014°C and 1042°C. To limit uncertainties on
597 the computed closure temperatures, we also calculated equilibrium temperatures between olivine and
598 clinopyroxene rims using the lattice strain model for REE and Y distribution among mantle minerals
599 (Sun and Liang, 2014). These equilibrium temperatures range between 1000°C and 1050°C
600 overlapping the computed closure temperatures. The duration required to generate a good fit to the
601 measured Ca profile represents a minimum timescale over which cooling might have occurred. The
602 higher-T and lower-T (< 900°C) history of cooling is outside the kinetic window of Ca, and thus the
603 total duration of cooling is longer than that calculated here via Ca-in-olivine cooling geospeedometry
604 (Fig. 5 and Supplementary Material Fig. S4).

605 The linear cooling rates obtained from the models span a range from 0.01 to 0.001 °C/yr (Fig. 6),
606 with a mean value of 0.004 °C/yr (Fig. 5 and Supplementary Material Fig. S4). Figure 6a displays data
607 from this study compared with downhole cooling rates of the oceanic crustal sequence from Hole
608 U1309D determined by combined U-Pb zircon crystallization ages, (U-Th)/He zircon
609 thermochronometry and multicomponent magnetic remanence data (Grimes et al., 2011;
610 Schoolmeesters et al., 2012). These cooling rates were determined at lower temperatures, from 780°C

611 to ~250°C. All data (this study; Grimes et al., 2011; Schoolmeesters et al., 2012) overlap within error,
612 showing that cooling rates are relatively constant with depth and time over a large range of
613 temperatures from magmatic conditions to present (Fig. 6a).

614

615 **5. Discussion**

616 *5.1 Preserved mantle chemical heterogeneities*

617 Reactive processes through oceanic crustal gabbros modify the composition of migrating melts and
618 pre-existing crystal matrix (e.g., Boulanger et al., submitted; Lissenberg et al., 2013; Lissenberg and
619 Dick, 2008). The spatial extent of these chemical modifications depends on the intensity of melt-rock
620 interactions, which are in turn strictly related to the frequency of magma inputs and the melt/rock ratio
621 (e.g., Basch et al., 2018; Higgie and Tommasi, 2012; Lambart et al., 2019; Fig.6). Continuous melt
622 infiltration at high melt/rock ratios and reactive melt transport can lead to progressive over-
623 enrichments in incompatible elements (Godard et al., 1995) from the deepest section of lower oceanic
624 crust to shallower levels (e.g., Hess Deep crustal sequence; Lissenberg et al., 2013). High melt/rock
625 ratios enable chemical homogenization and re-equilibration of the protolith minerals with the reacted
626 melt (Fig.6b) at the scale of few tens of meters. Extensive melt-rock interactions are able to shift the
627 composition of percolating melts towards the composition expected for fractionation of MORB at
628 elevated pressures (Lissenberg and Dick, 2008). On the other hand, episodic inputs of magma and low
629 melt-rock ratios integrated over time lead to changes in chemical composition of percolating melt and
630 crystal matrix at local, centimeter-scale (Basch et al., 2018; Fig. 7c), having a significant effect on the
631 geochemical budget of erupted basalts (Paquet et al., 2016).

632 The lack of up-hole over-enrichments (Fig. 1c) and the low-pressure magmatic differentiation
633 signature of Hole U1309D gabbroic section suggest that percolating melts were overall not chemically
634 modified by reactive porous flow at Atlantis Massif. Assuming continuous melt infiltration (e.g.,
635 beneath fast-spreading ridges), fast MT diffusive re-equilibration timescales (i.e., at magmatic
636 conditions) would be responsible of chemical homogeneity of olivines over tens of meters (Fig. 7b). In

637 contrast, the composition of olivines is heterogeneous throughout Hole U1309D, as evidenced by Ni
638 and Li (Fig. 1d), suggesting that the distribution of flow paths was confined into discrete intervals. The
639 strong variations in Ni and Li are inherited from pre-existing chemical heterogeneity of the mantle
640 protolith (Ferrando et al., 2018) and record local re-equilibration with the modified melt after the
641 reactive process (Fig. 7c) at relatively high melt/rock ratios.

642 The presence of Ol-Ts at different depths throughout Hole U1309D (Fig. 1c), together with their
643 inheritance of mantle heterogeneity and the fast MT diffusive re-equilibration of olivine crystals
644 modelled in this study, point to episodic small-scale magmatism. Although estimated re-equilibration
645 timescales are minimum durations, we document that Ol-Ts formed and cooled during the ongoing
646 uplift of the Atlantis Massif OCC (see *6.3 Role of detachment faults on crustal cooling*), suggesting
647 that they remain shortly at depth after formation.
648

649 *5.2 Depths of magma emplacement at Atlantis Massif*

650 Multiple episodes of magmatic infiltration triggered partial assimilation and incorporation of
651 lithospheric mantle slivers into the oceanic crust. Subsequently, the melts locally modified by mantle
652 partial assimilation migrated upwards and crystallized at variable depths to form gabbroic intrusions. It
653 is worth noting that modified melts likely represent only a portion of the parental magmas forming the
654 crustal sequence. Injections and crystallization of magma preserving their primary composition (i.e.,
655 not modified by reactive processes) also participated to the building of the lower oceanic crust at the
656 Atlantis Massif OCC. In the following, we use geothermometric estimates and cooling rates recorded
657 in rocks from Hole U1309D to reconstruct the history of formation and cooling of the oceanic crust at
658 the Atlantis Massif OCC.

659 Estimations of crystallization temperatures of the interstitial phases in Ol-Ts from the Atlantis
660 Massif (Drouin et al., 2009; Ferrando et al., 2018) indicate that melt-rock interactions occurred at
661 temperatures of ~1230°C. At such magmatic temperatures, our MT diffusive re-equilibration models
662 (Table 3; Fig. 4) demonstrate that pre-existing mantle olivine crystals are completely re-equilibrated

663 with the reactive percolating melt in either the time-frame of a single melt input (i.e. < 630 yrs
664 assuming the emplacement of a 10 m-thick sill; Grimes et al., 2008), or within the ~150 kyrs of
665 emplacement of the 635 m-thick deepest interval in Hole U1309D (i.e., between 600 and 1235 mbsf;
666 Grimes et al., 2008). Using 1230°C as formation temperature of Ol-Ts and the reconstruction of
667 isotherm depths previously documented at segment ends along the MAR (Grimes et al., 2011, 2008;
668 Schoolmeesters et al., 2012), we can predict the depth of Ol-Ts formation and mantle assimilation.
669 The depth of the ~900°C isotherm has been estimated to lay at 6-6.5 km beneath the ridge axis at
670 Atlantis Massif (Grimes et al., 2011, 2008; Schoolmeesters et al., 2012). Considering a geothermal
671 gradient of ~300-350°C/km at these depths (e.g., Grimes et al., 2011; Oxburgh and Turcotte, 1968),
672 we can extrapolate the 1230°C isotherm to lay at ~7.5-8 km depth during active magmatism beneath
673 the ridge (Fig. 8). This is consistent with the documented depth of clinopyroxene + plagioclase
674 crystallization front (i.e. double saturation at 8 km) beneath the axis of a slow-spreading ridge
675 (spreading rate ~20 mm/yr; Hebert and Montési, 2010).

676 Dissolution-precipitation reactions within the mantle require relatively high temperatures for the
677 reaction to prevail on melt crystallization (Kelemen, 1990); the efficiency of reactive processes thus
678 decreases with decreasing temperature. Combining our estimations of subsolidus cooling rates (Ca-in-
679 olivine: 0.004°C/yr; Fig. 6) and the OCC uplift rate of 15 mm/yr (Grimes et al., 2008), we estimate
680 ~700 m depth interval over which melt-rock interactions occurred and Ol-Ts formed and cooled from
681 1230°C to 1050-1100°C. Accordingly, we conclude that the 1050°C isotherm lies at 6.8-7.3 km depth
682 (Fig. 8).

683 At depths shallower than ~7 km (i.e., T<1050°C), melts are no longer modified by melt-rock
684 interactions and likely start to crystallize the gabbroic sills (Fig. 8). Nonetheless, Grimes et al. (2008)
685 and Schoolmeesters et al. (2012) estimated that most gabbroic sills are intruded in a rather cold
686 lithosphere (850°C), at 5-7 km depth. Therefore, Ol-Ts must have moved vertically to cool
687 conductively of additional ~200°C (from ~1050°C to ~850°C) before being intruded by the gabbro
688 parental magmas. Assuming that the position of isotherms was stable during magmatic activity at
689 Atlantis Massif, we performed calculations of the vertical displacement using uplift rates (15mm/yr)

690 associated to cooling duration of the Ol-T, using the cooling rates modelled in this study (0.004°C/yr,
691 Fig. 5 and Fig. 6). We estimate a vertical uplift of ~750 m from 1050°C to 850°C, for a total of 1.5km
692 during cooling of Ol-Ts from magmatic temperatures (1230°C, 7.5-8km depth) to cooler environments
693 (850°C). This indicates that Ol-Ts were located at 6-6.5km depth when gabbros formed (Fig. 8),
694 consistently with the depth of gabbroic intrusion estimated by Grimes et al. (2008) and
695 Schoolmeesters et al. (2012).

696 Taken as a whole, our results document an evolution from deep formation of Ol-Ts at 7.5-8 km
697 depth (1230°C) to their subsequent cooling to 1050°C at 6.8-7.3 km during constant uplift. From ~7
698 km depths at ~1050°C, reactive processes forming the Ol-Ts cease, and melt modified by melt-rock
699 interactions start crystallizing. The oldest intrusion event (1.24 Myr; Grimes et al., 2008) at Hole
700 U1309D was identified in the lower interval of the 1415 m-deep gabbroic section (below ~600 mbsf).
701 This suggests that the oldest intrusion event represents the deepest emplacement and early
702 crystallization of melts that were previously modified by reactive processes. The continuous
703 exhumation of the OCC by the detachment fault then brings the lower oceanic crustal section to 6-
704 6.5km depth (850°C), where younger and smaller intrusions (<10 m thick) are emplaced throughout
705 the Hole U1309D (Blackman et al., 2006; Grimes et al., 2008) and the Ol-Ts are integrated within the
706 gabbroic sequence.

707

708 *5.3 Role of detachment faults on crustal cooling*

709 Cooling rates retrieved from olivines in Ol-Ts from IODP Hole U1309D (Fig. 6a,b) are on average
710 0.004°C/yr (from Ca-in-olivine geospeedometry; Fig. 5 and Supplementary Material Fig. S4). These
711 cooling rates are comparable with cooling rates measured at different depths throughout the oceanic
712 crustal section from the same Hole, and obtained by U-Pb zircon crystallization ages combined with
713 (U-Th)/He zircon thermochronometry and multicomponent magnetic remanence data (Schoolmeesters
714 et al., 2012; Fig. 6a). The combination of Ca-in-olivine geospeedometry from this study and
715 previously published thermochronometric investigations document that cooling rates of the oceanic

crust exposed at the Atlantis Massif OCC are constant with depth (Fig. 6a). Moreover, cooling rates of the studied oceanic crustal section are not only constant in space (i.e., over depth), but also in time, as evidenced by similar cooling rates from high-temperature (1230-850°C; 0.004°C/yr; this study) to low temperature (850-250°C; 0.002-0.004°C/yr; Schoolmeesters et al., 2012). Comparable downhole constant cooling rates estimated using Ca-in-olivine geospeedometry have been determined for gabbroic rocks from a similar, but compositionally different OCC along the ultraslow-spreading SWIR (Atlantis Bank OCC; Coogan et al., 2007; Fig. 6c). One plausible explanation for constant cooling rates over space and time provided by Coogan et al. (2007) lies in the efficiency of crustal uplift in removing heat conductively. Also, John et al. (2004) determined cooling rates of the oceanic crust at the Atlantis Bank OCC using a different approach based on thermochronometric data. By applying a 2-D plate-cooling model for oceanic lithosphere, they demonstrated that the oceanic crust at an OCC mimics conductive cooling (at Atlantis Bank OCC over the temperature range ~900–330°C; John et al., 2004). Those cooling rates are comparable with cooling rates of the gabbroic sequence exposed at the Atlantis Massif OCC (Fig. 6c), which we thus infer to have cooled conductively.

Parental melts of the exposed gabbroic sequences (i.e., Atlantis Massif and Atlantis Bank OCCs) may have crystallized at depth within the lithosphere, and then cooled as the detachment fault transported the lower oceanic crust to shallower depths. In this scenario, conductive cooling would be simply controlled by the uplift rate (Coogan et al., 2007). To test this hypothesis we compare cooling rates of the Atlantis Massif with modelling of uplift-controlled cooling rates (modelling after Coogan et al., 2007; Fig 6b). Constant cooling rates of the studied oceanic crust can be reproduced by conductive cooling during constant uplift of the oceanic crust at rates of 10 to 20 mm/yr (Fig. 6b). This is consistent with the average vertical transport rate of 15 mm/yr estimated at the Atlantis Massif OCC by zircon thermochronometry (Grimes et al., 2008), and predicted by numerical models of oceanic crust accretion accommodated by detachment faulting at slow-spreading ridges (i.e., OCC; Tucholke et al., 2008). This simplified model suggests that denudation by detachment fault is able to cool conductively the oceanic crust.

742 The constant cooling rates point to continuous vertical transport of Ol-Ts induced by the Atlantis
743 Massif detachment fault (e.g., Canales et al., 2008; Cannat, 1996; Ildefonse et al., 2007; Tucholke et
744 al., 2008). The progressive uplift transported Hole U1309D crustal sequence from depths of ~6 km
745 (isotherm of ~850 °C) to ~1.5 km where gabbros passed through the ~250°C isotherm (zircon
746 thermochronometry estimations; Grimes et al., 2011; Schoolmeesters et al., 2012). Simple exhumation
747 calculations based on the downhole constant cooling rates (0.003-0.004°C/yr) and the constant
748 exhumation rate of 15mm/yr indicate that the oceanic crustal sequence has indeed been uplifted ~ 4-
749 4.5 km during its cooling from 850°C to 250°C (Fig. 8). The oldest gabbroic intrusions were likely
750 uplifted after their emplacement at depth and their cooling was driven by detachment fault-related
751 exhumation. Uplifting may not represent the sole mechanism of heat removal: magma emplacement in
752 a 'cold' lithosphere (<850°C) could account for fast and downhole constant cooling (e.g., Sleep and
753 Warren, 2014) for the youngest magma injection event.

754 Lower oceanic crust exposed at other OCCs, such as the Atlantis Bank (SWIR, 57°E; Coogan et
755 al., 2007; John et al., 2004; Fig. 6) and along the Fifteen- Twenty Fracture Zone (MAR, 14°N-16°N;
756 Grimes et al., 2011), also record fast and constant downhole cooling rates (0.002-0.005 °C/yr). The
757 latter are comparable to our estimates of cooling rates of the gabbroic sequence at the Atlantis Massif
758 OCC (0.004 °C/yr on average). These similarities suggest that denudation of oceanic crust by long-
759 lived detachment faults is able to remove heat from the slow-spreading lower oceanic crust worldwide.

760 Hydrothermalism is widely described along slow-spreading ridges (e.g., Boschi et al., 2008; Früh-
761 Green et al., 2016) and also affects cooling of the oceanic crust. Heat removal by fluid circulation is
762 well constrained in the upper section of lower oceanic crust at fast-spreading ridges (Hess Deep, East
763 Pacific Rise) and analogous ophiolites (Samail Ophiolite, Oman), where very fast cooling rates are
764 observed (Fig. 6c; Coogan et al., 2007; Faak and Gillis, 2016; Sun and Lissenberg, 2018). They are
765 significantly higher than those observed at OCCs. At OCCs, hydrothermal circulation appear to
766 dominantly affects rocks nearest to the detachment fault where higher permeability allows fluid
767 pathway (Hirose and Hayman, 2008); they undergo slow cooling (~0.0003 °C/yr; Schoolmeesters et
768 al., 2012) from 250°C to present day temperature. However, the presence of high-temperature

769 amphiboles downhole Hole U1309D (Blackman et al., 2006) suggests that hydrothermal convection
770 could contribute to heat removal at higher temperatures deeper in the section.

771

772 ## 6. Concluding remarks

773 Retrieving the timescales of magmatic processes leading to the formation of oceanic crust is crucial
774 for constraining magma supply at ridges and to understand the control of exhumation mechanisms on
775 cooling of the oceanic crust. We have shown that flat geochemical profiles in olivine can be used to
776 calculate minimum duration of complete re-equilibration of mantle olivine matrix with the melt
777 modified during melt-rock interactions. Despite mantle olivine can be completely re-equilibrated in
778 rather short timescales, textural and chemical heterogeneities of the precursor mantle are preserved at
779 the cm-scale throughout Hole U1309D. Such preserved small-scale heterogeneities rule out continuous
780 magma supply and indicate that magmatism at the Atlantis Massif OCC occurs as discrete melt inputs.
781 In this context, our minimum re-equilibration times (<300 years) estimated using multiple elements
782 demonstrate that mantle assimilation and formation of Ol-Ts can occur in the time-frame of a single
783 melt input. The lithospheric mantle is incorporated in the lower oceanic crust within the ~150 kyrs of
784 emplacement of the oldest and deepest magmatic interval in Hole U1309D. Subsequent subsolidus re-
785 equilibration during cooling of the gabbroic sequence from magmatic temperatures (1230°C) down to
786 1050°C was constrained for the first time at the Atlantis Massif OCC in this study; we estimated
787 cooling rates of 0.003-0.004 °C/yr.

788 These timescale estimations, combined with cooling rates at lower temperatures (from 850°C to
789 250°C) allow us to reconstruct the geodynamic evolution of Ol-Ts from their formation at depth to
790 their integration into the oceanic crustal sequence during continuous exhumation. At Atlantis Massif,
791 magma inputs at depth (7.5-8 km) assimilate discrete intervals of lithospheric mantle through reactive
792 porous flow processes, forming Ol-Ts. As detachment faulting initiates, Ol-Ts are transported to
793 shallower depths (at ~6-6.5 km) and concomitantly cool down to ~850°C. In this rather cold
794 environment, the reacted melts that previously formed the Ol-Ts start crystallizing. Subsequently, the

795 gabbroic sequence is continuously uplifted at a rate of ~15 mm/yr and cools conductively at constant
796 cooling rates.

797 The evolution of oceanic crust at OCC is controlled by the decreasing temperature of the uplifting
798 system. This decrease in temperature governs the rheology of the host rock and rules the ability of the
799 melt to react at depth (T > 1050°C) and to segregate into magmatic intrusions at lower temperatures (T
800 ~ 850°C). The constant downhole cooling rates from magmatic temperatures down to 250°C indicate
801 that the gabbroic sequence continuously formed and progressively cooled over ~150 ka, with no
802 apparent change in spreading and exhumation rates.

803

804 **Acknowledgements**

805 An anonymous Reviewer and M. Jollands are acknowledged for helpful comments and suggestions
806 that improved the manuscript. Also, we are grateful to M. Jollands for further constructive discussions.
807 The authors are thankful to T. Shea for initial model guidance. We thank A. Wallace for introduction
808 and access to the University of Delaware's High Performance Computing resources. The authors thank
809 B. Boyer and O. Bruguier for assistance on analytical instruments from the Microsonde Sud
810 (Géosciences Montpellier, University of Montpellier) and AETE-ISO platforms ("Analyses des
811 Elements en Trace dans l'Environnement et ISOtopes"; OREME observatory, University of
812 Montpellier) respectively. This project has been supported by the People Programme (Marie Curie
813 Actions) of the European Union's Seventh Framework Programme FP7/2007–2013/ under REA-Grant
814 Agreement No. 608001, 'ABYSS'. This research used samples and data provided by the Integrated
815 Ocean Drilling Program (IODP).

816

817 **References**

818 Basch, V., Rampone, E., Crispini, L., Ferrando, C., Ildefonse, B., Godard, M., 2019a. Multi-stage
819 Reactive Formation of Troctolites in Slow-spreading Oceanic Lithosphere (Erro – Tobbio , Italy):
820 a Combined Field and Petrochemical Study. J. Petrol. https://doi.org/10.1093/petrology/egz019.

821 Basch, V., Rampone, E., Borghini, G., Ferrando, C., Zanetti, A., 2019b. Origin of pyroxenites in the
822 oceanic mantle and their implications on the reactive percolation of depleted melts. Contrib. to
823 Mineral. Petrol. 174, 97. https://doi.org/10.1007/s00410-019-1640-0.

824 Basch, V., Rampone, E., Crispini, L., Ferrando, C., Ildefonse, B., Godard, M., 2018. From mantle
825 peridotites to hybrid troctolites : Textural and chemical evolution during melt-rock interaction
826 history. Lithos 323, 4–23. https://doi.org/10.1016/j.lithos.2018.02.025.

827 Bédard, J.H., 1993. Oceanic crust as a reactive filter: synkinematic intrusion, hybridization, and
828 assimilation in an ophiolitic magma chamber, western Newfoundland. Geology 21, 77–80.
829 https://doi.org/10.1130/0091-7613(1993)021<0077:OCAARF>2.3.CO;2

830 Bédard, J.H., Hébert, R., 1996. The lower crust of the Bay of Islands ophiolite, Canada: petrology,
831 mineralogy, and the importance of syntexis in magmatic differentiation in ophiolites and at ocean
832 ridges. J. Geophys. Res. 101, 25105–25124. https://doi.org/10.1029/96JB01343

833 Bédard, J.H., 2001. Parental magmas of Nain Plutonic Suite anorthosites and mafic cumulates: a trace
834 element modelling approach. Contrib. Mineral. Petrol. 141, 747–771.
835 https://doi.org/10.1007/s004100100268

836 Bindeman, I.N., Sigmarsson, O., Eiler, J., 2006. Time constraints on the origin of large volume basalts
837 derived from O-isotope and trace element mineral zoning and U-series disequilibria in the Laki and
838 Grímsvötn volcanic system. Earth Planet. Sci. Lett. 245, 245–259.
839 https://doi.org/10.1016/j.epsl.2006.02.029.

840 Blackman, D.K., Ildefonse, B., John, B.E., Ohara, Y., Miller, D.J., MacLeod, C.J., Scientists, and the
841 Expedition 304/305 Scientists, 2006. Expedition 304/305. Proceedings of the Integrated Ocean
842 Drilling Program 304/305. https://doi.org/10.2204/iodp.proc.304305.101.2006.

Blackman, D.K., Ildefonse, B., John, B.E., Ohara, Y., Miller, D.J., Abe, N., Abratis, M., Andal, E.S., Andreani, M., Awaji, S., Beard, J.S., Brunelli, D., Charney, A.B., Christie, D.M., Collins, J., Delacour, A.G., Delius, H., Drouin, M., Einaudi, F., Escartín, J., Frost, B.R., Früh-Green, G., Fryer, P.B., Gee, J.S., Godard, M., Grimes, C.B., Halfpenny, A., Hansen, H.E., Harris, A.C., Tamura, A., Hayman, N.W., Hellebrand, E., Hirose, T., Hirth, J.G., Ishimaru, S., Johnson, K.T.M., Karner, G.D., Linek, M., MacLeod, C.J., Maeda, J., Mason, O.U., McCaig, A.M., Michibayashi, K., Morris, A., Nakagawa, T., Nozaka, T., Rosner, M., Searle, R.C., Suhr, G., Tominaga, M., Handt, von der, A., Yamasaki, T., Zhao, X., 2011. Drilling constraints on lithospheric accretion and evolution at Atlantis Massif, Mid-Atlantic Ridge 30° N. J. Geophys. Res. 116, B07103. https://doi.org/10.1029/2010JB007931

Blackman, D.K., Karson, J.A., Kelley, D.S., Cann, J.R., Früh-Green, G.L., Gee, J.S., Hurst, S.D., John, B.E., Morgan, J., Nooner, S.L., Ross, D.K., Schroeder, T.J., Williams, E.A., 2002. Geology of the Atlantis Massif (Mid-Atlantic Ridge, 30° N): Implications for the evolution of an ultramafic oceanic core complex. Mar. Geophys. Res. 23, 443–469. https://doi.org/10.1023/B:MARI.0000018232.14085.75

Bloch, E.M., Jollands, M.C., Gerstl, S.S.A., Bouvier, A.S., Plane, F., Baumgartner, L.P., 2019. Diffusion of calcium in forsterite and ultra-high resolution of experimental diffusion profiles in minerals using local electrode atom probe tomography. Geochim. Cosmochim. Acta 265, 85-95. https://doi.org/10.1016/j.gca.2019.09.003.

Borghini, G., Francomme, J. E. & Fumagalli, P., 2018. Melt–dunite interactions at 0.5 and 0.7 GPa: experimental constraints on the origin of olivine-rich troctolites. Lithos 323, 44–57. https://doi.org/10.1016/j.lithos.2018.09.022

Boschi, C., Dini, A., Früh-Green, G.L., Kelley, D.S., 2008. Isotopic and element exchange during serpentinization and metasomatism at the Atlantis Massif (MAR 30°N): Insights from B and Sr isotope data. Geochim. Cosmochim. Acta 72, 1801–1823. https://doi.org/10.1016/j.gca.2008.01.013.

869 Brandl, P.A., Regelous, M., Beier, C., St, H., Neill, C.O., Nebel, O., Haase, K.M., 2016. The
870 timescales of magma evolution at mid-ocean ridges. Lithos, 240–243, 49–68.
871 https://doi.org/10.1016/j.lithos.2015.10.020.

872 Burgess, K. D., Cooper, R. F., 2013. Extended planar defects and the rapid incorporation of Ti^{4+} into
873 olivine. Contrib. to Mineral. Petrol. 166, 1223–1233. doi:10.1007/s00410-013-0918-x.

874 Canales, J.P., Tucholke, B.E., Xu, M., Collins, J.A., DuBois, D.L., 2008. Seismic evidence for large-
875 scale compositional heterogeneity of oceanic core complexes. Geochemistry, Geophys.
876 Geosystems 9. https://doi.org/10.1029/2008GC002009.

877 Cannat, M., Mével, C., Maia, M., Deplus, C., Durand, C., Gente, P., Agrinier, P., Belarouchi, A.,
878 Dubuisson, G, Humler, E., Reynolds, J., 1995. Thin crust, ultramafic exposures, and rugged
879 faulting patterns at the Mid-Atlantic Ridge (22°-24°N). Geology 23, 49–52.
880 https://doi.org/10.1130/0091-7613(1995)023<0049:TCUEAR>2.3.CO;2.

881 Cannat, M., 1996. How thick is the magmatic crust at slow spreading oceanic ridges? J. Geophys. Res.
882 101, 2847–2857. doi: 10.1029/95JB03116.

883 Chakraborty, S., 2008. Diffusion in Solid Silicates: A Tool to Track Timescales of Processes Comes
884 of Age. Annual Review of Earth and Planetary Sciences 36, 153–190.
885 doi:10.1146/annurev.earth.36.031207.124125.

886 Chakraborty, S., 2018. Diffusion Chronometry: Some Complications in an Emerging Tool. Eos Trans.
887 AGU, Fall Meet. Suppl., Abstract V34B-04.

888 Chamberlain, K.J., Morgan, D.J., Wilson, C.J.N., 2014. Timescales of mixing and mobilisation in the
889 Bishop Tuff magma body : perspectives from diffusion chronometry. Contrib. Mineral. Petrol.
890 168:1034. https://doi.org/10.1007/s00410-014-1034-2.

891 Cherniak, D.J., 2010. REE diffusion in olivine. Am. Mineral. 95, 362–368.
892 https://doi.org/10.2138/am.2010.3345.

893 Coogan, L.A., Hain, A., Stahl, S., Chakraborty, S., 2005. Experimental determination of the diffusion
894 coefficient for calcium in olivine between 900°C and 1500°C. Geochim. Cosmochim. Acta 69,
895 3683–3694. https://doi.org/10.1016/j.gca.2005.03.002.

896 Coogan, L.A., Jenkin, G.R.T., Wilson, R.N., 2007. Contrasting cooling rates in the lower oceanic crust
897 at fast- and slow-spreading ridges revealed by geospeedometry. J. Petrol. 48, 2211–2231.
898 https://doi.org/10.1093/petrology/egm057.

899 Coogan, L.A., Jenkin, G.R.T., Wilson, R.N., 2002. Constraining the cooling rate of the lower oceanic
900 crust: A new approach applied to the Oman ophiolite, Earth Planet. Sci. Lett. 199, 127–146.
901 https://doi.org/10.1016/S0012-821X(02)00554-X.

902 Coogan, L.A., O'Hara, M.J., 2015. MORB differentiation: In situ crystallization in replenished-tapped
903 magma chambers. Geochim. Cosmochim. Acta 158, 147–161.
904 https://doi.org/10.1016/j.gca.2015.03.010.

905 Costa, F., Dungan, M., 2005. Short time scales of magmatic assimilation from diffusion modeling of
906 multiple elements in olivine. Geology 33, 837–840. https://doi.org/10.1130/G21675.1.

907 Costa, F., Dohmen, R., Chakraborty, S., 2008. Time scales of magmatic processes from modeling the
908 zoning patterns of crystals. Rev. Min. & Geochem. 69, 545-594.
909 https://doi.org/10.2138/rmg.2008.69.14.

910 Crank, J., 1975. The Mathematics of Diffusion. Second edition. Oxford University Press Ely House,
911 London W.I.

912 D'Errico, M.E., Warren, J.M., Godard, M., 2016. Evidence for chemically heterogeneous Arctic
913 mantle beneath the Gakkel Ridge. Geochim. Cosmochim. Acta 174:291–312.
914 https://doi.org/10.1016/j.gca.2015.11.017.

915 Dodson, M.H., 1986. Closure Profiles in Cooling Systems. Mater. Sci. Forum 7, 145–154.
916 https://doi.org/10.4028/www.scientific.net/MSF.7.145.

917 Dodson, M.H., 1973. Closure temperature in cooling geochronological and petrological systems.
918 Contrib. to Mineral. Petrol. 40, 259–274. https://doi.org/10.1007/BF00373790.

919 Dohmen, R., Becker, H.W., Chakraborty, S., 2007. Fe-Mg diffusion in olivine I: experimental
920 determination between 700 and 1,200 °C as a function of composition, crystal orientation and
921 oxygen fugacity. Phys. Chem. Miner. 34:389–407. https://doi.org/10.1007/s00269-007-0157-7.

922 Dohmen, R., Chakraborty, S., 2007. Fe-Mg diffusion in olivine II: Point defect chemistry, change of
923 diffusion mechanisms and a model for calculation of diffusion coefficients in natural olivine. Phys.
924 Chem. Miner. 34, 409–430. https://doi.org/10.1007/s00269-007-0158-6.

925 Dohmen, R., Kasemann, S.A., Coogan, L., Chakraborty, S., 2010. Diffusion of Li in olivine. Part I:
926 experimental observations and a multi species diffusion model. Geochim. Cosmochim. Acta
927 74:274–292. https://doi.org/10.1016/j.gca.2009.10.016.

928 Drouin, M., Godard, M., Ildefonse, B., 2007. Origin of Olivine-Rich Troctolites from IODP Hole
929 U1309D in the Atlantis Massif (Mid-Atlantic Ridge): Petrostructural and Geochemical Study. Eos
930 Trans. AGU, 88(52), Fall Meet. Suppl., Abstract T53B-1300.

931 Drouin, M., Godard, M., Ildefonse, B., Bruguier, O., Garrido, C.J., 2009. Geochemical and
932 petrographic evidence for magmatic impregnation in the oceanic lithosphere at Atlantis Massif,
933 Mid-Atlantic Ridge (IODP Hole U1309D, 30°N). Chem. Geol. 264, 71–88.
934 https://doi.org/10.1016/j.chemgeo.2009.02.013.

935 Drouin, M., Ildefonse, B., Godard, M., 2010. A microstructural imprint of melt impregnation in slow
936 spreading lithosphere: Olivine-rich troctolites from the Atlantis Massif, Mid-Atlantic Ridge, 30°N,
937 IODP Hole U1309D. Geochemistry, Geophys. Geosystems 11, 1–21.
938 https://doi.org/10.1029/2009GC002995.

939 Escartín, J., Smith, D.K., Cann, J., Schouten, H., Langmuir, C.H., Escrig, S., 2008. Central role of
940 detachment faults in accretion of slow-spreading oceanic lithosphere. Nature 455, 790–794.
941 doi:10.1038/nature07333.

942 Faak, K., Chakraborty, S., Coogan, L.A., 2013. Mg in plagioclase: Experimental calibration of a new
943 geothermometer and diffusion coefficients. Geochim. Cosmochim. Acta 123, 195–217.
944 https://doi.org/10.1016/j.gca.2013.05.009.

945 Faak, K., Gillis, K.M., 2016. Slow cooling of the lowermost oceanic crust at the fast-spreading East
946 Pacific Rise. Geology 44, 115–118. https://doi.org/10.1130/G37353.1.

947 Ferrando, C., Godard M., Ildefonse B., Rampone E., 2018. Melt transport and mantle assimilation at
948 Atlantis Massif (IODP Site U1309): Constraints from geochemical modeling. Lithos 323,
949 https://doi.org/10.1016/j.lithos.2018.01.012.

950 Früh-Green, G.L., Orcutt, B.N., Green, S.L., Cotterill, C., and the Expedition 357 Scientists (2016).
951 Expedition 357 Preliminary Report: Atlantis Massif Serpentinization and Life, International Ocean
952 Discovery Program, 357. http://dx.doi.org/10.14379/iodp.pr.357.2016.

953 Godard, M., Awaji, S., Hansen, H., Hellebrand, E., Brunelli, D., Johnson, K., Yamasaki, T., Maeda, J.,
954 Abratis, M., Christie, D., Kato, Y., Mariet, C., Rosner, M., 2009. Geochemistry of a long in-situ
955 section of intrusive slow-spread oceanic lithosphere: Results from IODP Site U1309 (Atlantis
956 Massif, 30°N Mid-Atlantic-Ridge). Earth Planet. Sci. Lett. 279, 110–122.
957 https://doi.org/10.1016/j.epsl.2008.12.034.

958 Godard, M., Bodinier, J.-L., Vasseur, G. (1995). Effects of mineralogical reactions on trace element
959 redistributions in mantle rocks during percolation processes: A chromatographic approach. Earth
960 Planet. Sci. Lett. 133, 449–461. doi:10.1016/0012-821X(95)00104-K.

961 Grimes, C.B., Cheadle, M.J., John, B., Reiners, P.W., Wooden, J.L., 2011. Cooling Rates and the
962 Depth of Detachment Faulting At Oceanic Core Complexes : Evidence from Zircon Pb/U and (U-
963 Th)/He Ages Pb/U and (U- Th)/He ages. Geochemistry Geophys. Geosystems 12, 1525- 2027.
964 https://doi.org/10.1029/2010GC003391.

965 Grimes, C.B., John, B.E., Cheadle, M.J., Wooden, J.L., 2008. Protracted construction of gabbroic crust
966 at a slow spreading ridge: Constraints from 206Pb/238U zircon ages from Atlantis Massif and

967 IODP Hole U1309D (30°N, MAR). Geochemistry, Geophys. Geosystems 9.
968 https://doi.org/10.1029/2008GC002063.

969 Günther, D. and Heinrich, C., 1999. Enhanced sensitivity in laser ablation-ICP mass spectrometry
970 using helium-argon mixtures as aerosol carrier. Journal of Analytical Atomic Spectrometry, 14,
971 1363–1368. https://doi.org/10.1039/A901648A.

972 Hebert, L.B., Montési, L.G.J., 2010. Generation of permeability barriers during melt extraction at mid-
973 ocean ridges. Geochemistry, Geophys. Geosystems 11, 1–17.
974 https://doi.org/10.1029/2010GC003270.

975 Ildefonse, B., Blackman, D.K., John, B.E., Ohara, Y., Miller, D.J., MacLeod, C.J., Abe, N., Abratis,
976 M., Andal, E.S., Andréani, M., Awaji, S., Beard, J.S., Brunelli, D., Charney, A.B., Christie, D.M.,
977 Delacour, A.G., Delius, H., Drouin, M., Einaudi, F., Escartin, J., Frost, B.R., Fryer, P.B., Gee, J.S.,
978 Godard, M., Grimes, C.B., Halfpenny, A., Hansen, H.E., Harris, A.C., Hayman, N.W., Hellebrand,
979 E., Hirose, T., Hirth, J.G., Ishimaru, S., Johnson, K.T.M., Karner, G.D., Linek, M., Maeda, J.,
980 Mason, O.U., McCaig, A.M., Michibayashi, K., Morris, A., Nakagawa, T., Nozaka, T., Rosner, M.,
981 Searle, R.C., Suhr, G., Tamura, A., Tominaga, M., von der Handt, A., Yamasaki, T., Zhao, X.,
982 2007. Oceanic core complexes and crustal accretion at slow-spreading ridges. Geology 35, 623–
983 626. https://doi.org/10.1130/G23531A.1.

984 Ito, M., Yurimoto, H., Morioka, M., Nagasawa, H., 1999. Co^{2+} and Ni^{2+} diffusion in olivine
985 determined by secondary ion mass spectrometry. Phys. Chem. Miner. 26, 425–431.

986 John, B.E., Foster, D.A., Murphy, J.M., Cheadle, M.J., Baines, A.G., Fanning, C.M., Copeland, P.,
987 2004. Determining the cooling history of in situ lower oceanic crust-Atlantis Bank, SW Indian
988 Ridge. Earth Planet. Sci. Lett. 222, 145–160. https://doi.org/10.1016/j.epsl.2004.02.014.

989 Jollands, M.C., Hermann, J., O'Neill, H.S.C., Spandler, C., Padrón-Navarta, J.A., 2016. Diffusion of
990 Ti and some Divalent Cations in Olivine as a Function of Temperature, Oxygen Fugacity,

991 Chemical Potentials and Crystal Orientation. J. Petrol. 57, 1983–2010.
992 doi:10.1093/petrology/egw067.

993 Jollands, M. C., Müntener, O., 2019. Testing Orthopyroxene Diffusion Chronometry on Rocks From
994 the Lanzo Massif (Italian Alps). J. Geoph. Res.: Solid Earth 1–20.
995 https://doi.org/10.1029/2018jb016963.

996 Kelemen, P.B., 1990. Reaction between Ultramafic rock and fractionating basaltic magma I. Phase
997 relations, the origin of calc-alkaline magma series, and the formation of discordant dunite. J. Petrol.
998 31, 51-98.

999 Köhler, T.P., Brey, G.P., 1990. Calcium exchange between olivine and clinopyroxene calibrated as a
1000 geothermobarometer for natural peridotites from 2 to 60 kb with applications. Geochim.
1001 Cosmochim. Acta 54, 2375–2388. https://doi.org/10.1016/0016-7037(90)90226-B.

1002 Kress, V.C., Ghiorso, M.S., 1995. Multicomponent diffusion in basaltic melts. Geochim. Cosmochim.
1003 Acta, 59, 313-324.

1004 Lambart, S., Koornneef, J.M., Millet, M.-A., Davies G.R., Cook, M., Lissenberg, C.J., 2019. Highly
1005 heterogeneous depleted mantle recorded in the lower oceanic crust. Nat. Geosc. 12, 482-486.
1006 https://doi.org/10.1038/s41561-019-0368-9.

1007 Lissenberg, C.J., Dick, H.J.B., 2008. Melt-rock reaction in the lower oceanic crust and its implications
1008 for the genesis of mid-ocean ridge basalt. Earth Planet. Sci. Lett. 271, 311–325.
1009 https://doi.org/10.1016/j.epsl.2008.04.023.

1010 Lissenberg, C.J., MacLeod, C.J., Howard, K.A., Godard, M., 2013. Pervasive reactive melt migration
1011 through fast-spreading lower oceanic crust (Hess Deep, equatorial Pacific Ocean). Earth Planet.
1012 Sci. Lett. 361, 436–447. https://doi.org/10.1016/j.epsl.2012.11.012.

1013 Lissenberg, C. J., MacLeod, C. J., 2016. A reactive porous flow control on mid-ocean ridge magmatic
1014 evolution. J. Petr. 57, 2195–2220. https://doi.org/10.1093/petrology/egw074.

1015 Lissenberg, C.J., MacLeod, C.J., Bennett E.N., 2019. Consequences of a crystal mush-dominated
1016 magma plumbing system: a mid-ocean ridge perspective. Philos. Trans. R. Soc. A 377:2139.
1017 https://doi.org/10.1098/rsta.2018.0014.

1018 Lynn, K.J., Garcia, M.O., Shea, T., Costa, F., Swanson, D.A., 2017a. Timescales of mixing and
1019 storage for Keanakāko‘i Tephra magmas (1500–1820 C.E.), Kīlauea Volcano, Hawai‘i. Contrib. to
1020 Mineral. Petrol. 172:76. https://doi.org/10.1007/s00410-017-1395-4.

1021 Lynn, K.J., Shea, T., Garcia, M.O., 2017b. Nickel variability in Hawaiian olivine: Evaluating the
1022 relative contributions from mantle and crustal processes. Am. Mineral. 102, 507–518.
1023 https://doi.org/10.2138/am-2017-5763.

1024 Lynn, K.J., Shea, T., Garcia, M.O., Costa, F., Norman, M.D., 2018. Lithium diffusion in olivine
1025 records magmatic priming of explosive basaltic eruptions. Earth Planet. Sci. Lett. 500, 127–135.
1026 https://doi.org/10.1016/j.epsl.2018.08.002.

1027 Nakamura, M., 1995. Residence time and crystallization history of nickeliferous olivine phenocrysts
1028 from the northern Yatsugatake volcanoes, Central Japan: Application of a growth and diffusion
1029 model in the system Mg-Fe-Ni. J. Volcanol. Geotherm. Res. 66, 81–100.
1030 https://doi.org/10.1016/0377-0273(94)00054-K.

1031 O'Hara,M.J., 1977. Geochemical evolution during fractional crystallisation of a periodically refilled
1032 magma chamber. Nature 266, 503–507.

1033 O’Neill, H., Jenner, F.E., 2012. The global pattern of trace-element distributions in ocean floor basalts.
1034 Nature 491, 698–704. https://doi.org/10.1038/nature11678.

1035 Oxburgh, E.R., Turcotte, D.L., 1968. Mid-Ocean Ridges and Geotherm Distribution during Mantle
1036 Convection. J. Geophys. Res. 73.

1037 Paquet,M., Cannat,M., Brunelli, D., Hamelin, C., Humler, E., 2016. Effect of melt/mantle interactions
1038 on MORB chemistry at the easternmost Southwest Indian Ridge (61°–67°E). Geochem. Geophys.
1039 Geosyst. 17. https://doi.org/10.1002/2016GC006385.

1040 Pearce, N.J.G., Perkins, W.T., Westgate, J.A., Gorton, M.P., Jackson, S.E., Neal, C.R., Chenery, S.P.,
1041 1997. A compilation of new and publishedmajor and trace element data for NIST SRM 610 and
1042 NIST SRM 612 glass reference materials. Geostandards Newsletter: The Journal of Geostandards
1043 and Geoanalysis 21 (1), 115–144.

1044 Petry, C., Chakraborty, S., Palme, H., 2004. Experimental determination of Ni diffusion coefficients in
1045 olivine and their dependence on temperature, composition, oxygen fugacity, and crystallographic
1046 orientation. Geochim. Cosmochim. Acta 68, 4179–4188. https://doi.org/10.1016/j.gca.2004.02.024.

1047 Rampone, E., Borghini, G., Basch, V., 2020. Melt migration and melt-rock reaction in the Alpine-
1048 Apennine peridotites : Insights on mantle dynamics in extending lithosphere. Geosci. Front. 11(1),
1049 151-166. https://doi.org/10.1016/j.gsf.2018.11.001.

1050 Rampone, E., Borghini, G., Godard, M., Ildefonse, B., Crispini, L., Fumagalli, P., 2016. Melt/rock
1051 reaction at oceanic peridotite/gabbro transition as revealed by trace element chemistry of olivine.
1052 Geochim. Cosmochim. Acta 190, 308-331.

1053 Regelous, M., Weinzierl, C., Haase, K., 2016. Controls on melting at spreading ridges from correlated
1054 abyssal peridotite - mid-ocean ridge basalt compositions. Earth Planet. Sci. Lett., 449, 1-11.
1055 https://dx.doi.org/10.1016/j.epsl.2016.05.017.

1056 Roeder, P.L., Emslie, R.F., 1970. Olivine-Liquid Equilibrium. Contr. Miner. Pet. 29, 275–289.

1057 Sanfilippo, A., Morishita, T., Kumagai, H., Nakamura, K., Okino, K., Hara, K., Tamura, A., Arai, S.,
1058 2015. Hybrid troctolites from mid-ocean ridges: Inherited mantle in the lower crust. Lithos 232,
1059 124–130. https://doi.org/10.1016/j.lithos.2015.06.025.

1060 Sanfilippo, A., Tribuzio, R., Tiepolo, M., 2014. Mantle-crust interactions in the oceanic lithosphere:
1061 Constraints from minor and trace elements in olivine. Geochim. Cosmochim. Acta 141, 423–439.
1062 https://doi.org/10.1016/j.gca.2014.06.012.

1063 Schoolmeesters, N., Cheadle, M.J., John, B.E., Reiners, P.W., Gee, J., Grimes, C.B., 2012. The
1064 cooling history and the depth of detachment faulting at the Atlantis Massif oceanic core complex.
1065 Geochemistry, Geophys. Geosystems 13, 1–19. https://doi.org/10.1029/2012GC004314.

1066 Shea, T., Costa, F., Krimer, D., Hammer, J.E., 2015. Accuracy of timescales retrieved from diffusion
1067 modeling in olivine: A 3D perspective. Am. Mineral. 100, 2026–2042. https://doi.org/10.2138/am-
1068 2015-5163.

1069 Sleep, N.H., Warren, J.M., 2014. Effect of latent heat of freezing on crustal generation at low
1070 spreading rates. Geochemistry Geophys. Geosystems 15, 3161–3174.
1071 https://doi.org/10.1002/2014GC005423.

1072 Spandler, C., O'Neill, H.S.C., 2010. Diffusion and partition coefficients of minor and trace elements
1073 in San Carlos olivine at 1,300°C with some geochemical implications. Contrib. to Mineral. Petrol.
1074 159, 1–28. https://doi.org/10.1007/s00410-009-0456-8.

1075 Suhr, G., Hellebrand, E., Johnson, K., Brunelli, D., 2008. Stacked gabbro units and intervening
1076 mantle: A detailed look at a section of IODP Leg 305, Hole U1309D. Geochemistry, Geophys.
1077 Geosystems 9. https://doi.org/10.1029/2008GC002012.

1078 Sun, C., Liang, Y., 2014. An assessment of subsolidus re-equilibration on REE distribution among
1079 mantle minerals olivine, orthopyroxene, clinopyroxene, and garnet in peridotites. Chem. Geol. 372,
1080 80–91. https://doi.org/10.1016/j.chemgeo.2014.02.014.

1081 Sun, C., Liang, Y., 2012. Distribution of REE between clinopyroxene and basaltic melt along a mantle
1082 adiabat: Effects of major element composition, water, and temperature. Contrib. to Mineral. Petrol.
1083 163, 807–823. https://doi.org/10.1007/s00410-011-0700-x.

1084 Sun, C., Lissenberg, C.J., 2018. Formation of fast-spreading lower oceanic crust as revealed by a new
1085 Mg–REE coupled geospeedometer. Earth Planet. Sci. Lett.487, 165–178.
1086 https://doi.org/10.1016/j.epsl.2018.01.032

1087 Tamura, A., Arai, S., Ishimaru, S., Andal, E.S., 2008. Petrology and geochemistry of peridotites from
1088 IODP Site U1309 at Atlantis Massif, MAR 30°N: Micro- and macro-scale melt penetrations into
1089 peridotites. Contrib. to Mineral. Petrol. 155, 491–509. https://doi.org/10.1007/s00410-007-0254-0.

1090 Tucholke, B.E., Behn, M.D., Buck, W.R., Lin, J., 2008. Role of melt supply in oceanic detachment
1091 faulting and formation of megamullions. Geology 36, 455–458.
1092 https://doi.org/10.1130/G24639A.1.

1093 Van Achterberg, E., Ryan, C.G., Jackson, S.E., Griffin, W., 2001. Data reduction software for LA-
1094 ICP-MS. In: Sylvester, P. (Ed.), Laser ablation ICP-MS in the Earth Science. Mineralogical
1095 Association of Canada, pp. 239–243.

1096 Van Orman, J. A., Grove, T. L. & Shimizu, N., 2001. Rare earth element diffusion: influence of
1097 temperature, pressure, and ionic radius, and an elastic model for diffusion in silicates. Contrib. to
1098 Mineral. Petrol. 141, 687–703. https://doi.org/10.1007/s004100100269.

1099 Witt-Eickschen, G., O'Neill, H.S.C., 2005. The effect of temperature on the equilibrium distribution of
1100 trace elements between clinopyroxene, orthopyroxene, olivine and spinel in upper mantle
1101 peridotite. Chem. Geol. 221, 65–101. https://doi.org/10.1016/j.chemgeo.2005.04.005.

1102 Yang, A.Y., Wang, C., Liang, Y., Lissenberg, C.J., 2019. Reaction between mid- ocean ridge basalt
1103 and lower oceanic crust: an experimental study. Geochem. Geophys. Geosys. 20, 4390-4407.
1104 https://doi.org/10.1029/2019GC008368.

1105 Zhang, X., Ganguly, J., Ito, M., 2010. Ca-Mg diffusion in diopside: Tracer and chemical interdiffusion
1106 coefficients. Contrib. to Mineral. Petrol. 159, 175–186. https://doi:10.1007/s00410-009-0422-5.

1107

1108 **Figures and Tables captions**

1109 **Figure 1 (two columns)** - (a) Location of the Atlantis Massif OCC at 30°N on the MAR and
1110 topography of the Atlantis Transform Fault region (modified from Blackman et al., 2006). (b)

1111 Examples of recovered intervals of (left) Ol-T1 (Core 248R-3, 82–104 cm) composed of wehrlitic
1112 (WEHRL), troctolitic (TROCT) and minor dunitic (DUN) domains, and (right) Ol-T2 (Core 248R-2,
1113 5–26 cm) mainly composed of plagioclase-dunitic domains and cut by a gabbroic vein. (c) Downhole
1114 composition of IODP Hole U1309D (from left to right): 20 m running average of rock type recovered
1115 (white indicates no recovery), variations in whole-rock Mg # (Mg# (cationic ratio) =
1116 100×Mg/(Mg+Fetotal); modified after Blackman et al., 2006), and Zircon Pb/U Ages where numbers
1117 indicate averages of measurements (Grimes et al., 2008). (d) Ni and Li average composition of olivine
1118 from single samples of Ol-Ts selected for this study in the interval 1100–1200 mbsf.

1119

1120 **Figure 2 (two columns)** - Chemical profiles across olivine crystals for Mg#, NiO wt%, Co (ppm), Zn
1121 (ppm), CaO wt%, Y (ppm) and Yb (ppm). Sample name and location of relative profile on single
1122 olivine are reported on top. Orange dots are used for Ol-T1 and red for Ol-T2.

1123

1124 **Figure 3 (one column)** - (a) 3D numerical olivine used in the models. Dashed white line indicates 2D
1125 section taken perpendicular to the c-axis [001]. Models were run twice, with 1 and 3 mm c-axis
1126 lengths. (b) Initial olivine (C_0) and melt (C_i=C1) compositions used in the models. An initially
1127 homogeneous crystal with a sharp compositional boundary to the surrounding melt was then allowed
1128 to diffuse at the conditions specified for each model and element.

1129

1130 **Figure 4 (two colmns)** - Results of MT diffusive re-equilibration model to simulate timescales of
1131 melt-rock interactions at 1230 ±20°C (a-b) and 1300°C (c) using C_0a as starting olivine composition
1132 (Table B2). (a-c) Evolution of the modeled % re-equilibration (% req) of olivine core as function of
1133 time of re-equilibration (years). Symbols represent olivine grain size of 1 mm and lines are for grain
1134 size of 4 mm. Colors distinguish each modelled element and reported in the legend. The time of re-
1135 equilibration is compared with the time of emplacement of a single 10 m thick sill (~630 years, light

1136 grey) after Grimes et al. (2008). In (a) shaded areas in green, Co, and black, Ni, represent the ±Δ in
1137 time of re-equilibration ($\pm\Delta t_T$) at given % req related to uncertainties in crystallization temperature
1138 (Drouin et al., 2009). They are reported for Co and Ni in 1 mm models only to provide examples; $\pm\Delta t_T$
1139 of all other elements can be found in Table 3. (b) 1D rim-to-rim profile evolution along the *a*-axis
1140 across 1 mm sized olivine (see Appendix 2 for procedure of 1D profile sampling) are reported for Fo,
1141 NiO (wt%) and MnO (wt%) from MT diffusive re-equilibration model at 1230°C.. Colored lines
1142 (elements are represented by colors as reported in the legend) highlight olivine composition after 50%
1143 of diffusive re-equilibration and olivine composition at effective % req (marked with * in the legend).
1144 For details on the MT diffusive re-equilibration models see the text and Appendix 2.

1145

1146 **Figure 5 (one column)** - Ca profile in olivine from sample 305-U1309D-248R-3W, 36-38. Plotted
1147 lines are Ca-cooling model at increasing time step as reported in the legend. The initial composition is
1148 represented by the dotted black line. The cooling rate calculate from this Ca profile corresponds to
1149 0.004 °C/yr. For details on the Ca-in-olivine geospeedometry see the text and Appendix 4.

1150

1151 **Figure 6 (one column)** - Cooling rates (°C/year) obtained from Ca-in-olivine geospeedometry on Ol-
1152 Ts from this study (orange dots, Ol-T1, and red dots, Ol-T2) compared with cooling rates of slow- and
1153 fast-spreading oceanic crust. (a) Dots are downhole Hole U1309D cooling rates determined for
1154 gabbroic rocks by combined U-Pb zircon crystallization ages and (U-Th)/He zircon
1155 thermochronometry (Grimes et al., 2011) and multicomponent magnetic remanence data
1156 (Schoolmeesters et al., 2012). For the latter, we selected initial cooling rates (780°C-250°C) to ignore
1157 the effect of late-stage hydrothermal circulation, which buffer temperatures and decreases the cooling
1158 rates to ~0.0003 °C/yr (Schoolmeesters et al., 2012). The dotted blue box indicates the depth interval
1159 in (b). (b) Zoom-in of the studied interval (1190-1196 mbsf). Dotted black lines indicate constant
1160 downhole conductive cooling during uplift toward the surface modelled assuming temperatures of 0°C
1161 at surface and 1300°C at depth of magma emplacement (model from Coogan et al., 2007). Models of

conductive cooling are reported for uplift rates of 10 and 20 mm/year. (c) Ranges of cooling rates of the *(i)* slow-spread oceanic crustal section at Atlantis Bank OCC (black bars) retrieved using Ca-in-olivine geospeedometry (Atlantis Bank OCC and another OCC along the Mid Atlantic Ridge at 23°N (MARK area); Coogan et al., 2007) and thermochronometric data (John et al., 2004), and *(ii)* shallower section of the fast-spread crustal sequence at Hess Deep Rift (grey bar; Coogan et al.; 2007 Faak and Gillis, 2016; Sun and Lissenberg, 2018).

Figure 7 (two columns) - Schematic view of two different melt percolation styles leading to mantle assimilation of a common pre-existing heterogeneous harzburgite (a). (b) Continuous magma income leads to homogenization of olivines composition over a scale of few tens of meters. (c) Episodic magma inputs modify the chemical composition of percolating melt and crystal matrix at local centimeter-scale. Olivine color indicates olivine Mg# and NiO (wt%) composition as reported in the legend.

Figure 8 (two columns) - Interpretative sketch of the structure of the oceanic crust formed at the Atlantis Massif OCC. The thermal reconstruction is proposed based on diffusive re-equilibration and cooling modelling.

Table 1 - Selected olivine diffusion coefficients (m^2/s) reported in logarithmic scale; T ≈ 1200-1300°C and Fo ≈ 92. Diffusion coefficients were measured along the axis reported on top of each column ([100], [010], [001] are respectively a-axis, b-axis, c-axis). [1] Dohmen et al. (2007); [2] Petry et al. (2004); [3] Ito et al. (1999); [4] Spandler and O'Neill (2010); [5] Coogan et al. (2005); [6] Cherniak (2010); * single value at 1300°C; ** average between [010] and [001]; *** anisotropy not considered.

Table 2 - List of samples and their principal textural characteristics and mineral chemical compositions. Ol=olivine, Spl=spinel, Cpx=clinopyroxene, Plg=plagioclase. Mg#=100×cationic (Mg/(Mg+Fe), with all Fe as Fe^{2+}.

Table 3 - Timescales (yr = years) of chemical re-equilibration, after mantle-melt interactions; % req is the effective % req (see text for details). Millimeters (mm) refer to the diameter of modelled olivine. Δt_T is the difference between timescales calculated at 1210°C (t_{1210}), 1230°C (t_{1230}), 1250°C (t_{1250}) ($+\Delta t_T = t_{1210} - t_{1230}$; $-\Delta t_T = t_{1250} - t_{1230}$). Δt_X ($|\Delta t_X|$) is the difference between timescales calculated using two different starting olivine composition C_0a and C_0b.

Appendices

Appendix A

Simulations of *MT diffusive re-equilibration* were performed using three solutions of the three-dimensional form of Fick's second law (Crank, 1975). The concentration dependent equation for anisotropic diffusing species was used for Fe-Mg, Ni, and Mn:

$$\frac{\partial C_i}{\partial t} = \left[\frac{\partial}{\partial x}\left(D_x \frac{\partial C_i}{\partial x}\right) + \frac{\partial}{\partial y}\left(D_y \frac{\partial C_i}{\partial y}\right) + \frac{\partial}{\partial z}\left(D_z \frac{\partial C_i}{\partial z}\right)\right] \quad \text{(A1)}$$

where C_i is the concentration of element *i* (ppm or wt%), *t* is time (s), and D_x, D_y and D_z are the diffusion coefficients (m^2 s^{-1}) of element *i* along the principal crystallographic axes [100], [010] and [001], noted in x, y, and z dimensions, respectively. The MT diffusive re-equilibration models of Ni and Mn were run concurrently with Fe-Mg models to account for the concentration dependence of these elements on the olivine Fo content. Diffusive re-equilibration of Ca was modeled using the non-concentration dependent form for anisotropic diffusion:

$$\frac{\partial C_i}{\partial t} = \left[D_x\left(\frac{\partial^2 C_i}{\partial x^2}\right) + D_y\left(\frac{\partial^2 C_i}{\partial y^2}\right) + D_z\left(\frac{\partial^2 C_i}{\partial z^2}\right)\right] \quad \text{(A2)}$$

and trace elements (Co, Dy, La, Y, Lu, Zn) were modeled using the non-concentration dependent form for isotropic diffusion:

$$\frac{\partial C_i}{\partial t} = D_i \left[\left(\frac{\partial^2 C_i}{\partial x^2} \right) + \left(\frac{\partial^2 C_i}{\partial y^2} \right) + \left(\frac{\partial^2 C_i}{\partial z^2} \right) \right] \quad \text{(A3)}$$

For the *Ca-in-olivine geospeedometry* we used a non-concentration dependent 1D form of Fick's second law:

$$\frac{\partial C_i}{\partial t} = D_i \left(\frac{\partial^2 C_i}{\partial x^2} \right) \quad \text{(A4)}$$

We utilized the simplified diffusion coefficient for Ca in olivine (D_{Ca}) from Coogan et al. (2005):

$$\log D = \log \left[D_o \exp \left(\frac{-E}{RT} \right) \right] + 0.31 \Delta \log fO_2 \quad \text{(A5)}$$

where D_o is the preexponential factor (m^2/s), E is the activation energy (kJ/mol), R is the gas constant, T is temperature (K), and fO_2 is the oxygen fugacity.

Appendix B

Table B1 - Diffusivities utilized by 3D diffusion models. D = diffusion coefficient, m^2/s; T = temperature, Kelvin; P = pressure and fO_2 = oxygen fugacity, Pascals; X_{Fe} = mole fraction of the fayalite; R = gas constant, J/mol/K.

Element	Diffusivity Equation*	Reference
Fe-Mg, Mn	$D_c = 10^{-9.21} \left(\frac{f_{O2}}{10^{-7}} \right)^{\frac{1}{6}} 10^{3(X_{Fe}-0.1)} \exp \left(\frac{-201000+(P-10^5)(7\times10^{-6})}{RT} \right)$ $D_a = D_b = \frac{1}{6} D_c$	Dohmen and Chakraborty (2007)
Ni	$D_c = 3.84\times10^{-9} \left(\frac{f_{O2}}{10^{-6}} \right)^{\frac{1}{4.25}} 10^{1.5(X_{Fe}-0.1)} \exp \left(\frac{-220000+(P-10^5)(7\times10^{-6})}{RT} \right)$ $D_a = D_b = \frac{1}{6} D_c$	Petry et al. (2004)
Ca	$D_a = 16.59\times10^{-12} \left(\frac{f_{O2}}{10^{-7}} \right)^{\frac{1}{3.2}} \exp \left(\frac{-193000}{RT} \right)$ $D_b = 34.67\times10^{-12} \left(\frac{f_{O2}}{10^{-7}} \right)^{\frac{1}{3.2}} \exp \left(\frac{-201000}{RT} \right)$ $D_c = 95.49\times10^{-12} \left(\frac{f_{O2}}{10^{-7}} \right)^{\frac{1}{3.2}} \exp \left(\frac{-207000}{RT} \right)$	Coogan et al. (2005)
Co	$D = 5.59\times10^{-5} \exp \left(\frac{-328000}{RT} \right)$	Ito et al. (1999)

Dy, La	$D = 8\times10^{-10}\exp\left(\frac{-289000}{RT}\right)$	Cherniak (2010)
Y	$D = 10^{-15.23}$ *single D value at 1300°C*	Spandler and O'Neill (2010)
Lu	$D = 10^{-15.38}$ *single D value at 1300°C*	Spandler and O'Neill (2010)
Zn	$D = 10^{-14.75}$ *single D value at 1300°C*	Spandler and O'Neill (2010)

Table B2 - Initial and boundary conditions of 3D model. C_0a is the average composition of harzburgite olivine from Gakkel Ridge (D'Errico et al., 2016; Regelous et al., 2016). C_0b the same initial composition of a single harzburgite olivine used by Ferrando et al. (2018).

Element	**C_0a (initial condition)**	**C_0b (initial condition)**	**C1 (boundary condition) - averages of EPMA and LA-ICP-MS measurements in Ol-T 1**
FeMg (Fo)	91 +/- 0.9 mol%	92 mol%	85 mol%
Ni	0.26 +/- 0.05 wt%	0.26 wt%	0.30 wt%
Zn	53 +/- 6 ppm	55 ppm	75 ppm
Mn	0.15 +/- 0.03 wt%	0.11 wt%	0.24 wt%
Co	153 +/- 8 ppm	125 ppm	160 ppm
Ca	0.1 +/- 0.05 wt%	0.105 wt%	0.09 wt%
Y	0.0032 +/- 0.002 ppm	0.001 ppm	0.10 ppm
Lu	0.0028 +/- 0.002 ppm	0.0041 ppm	0.015 ppm

Figure 1

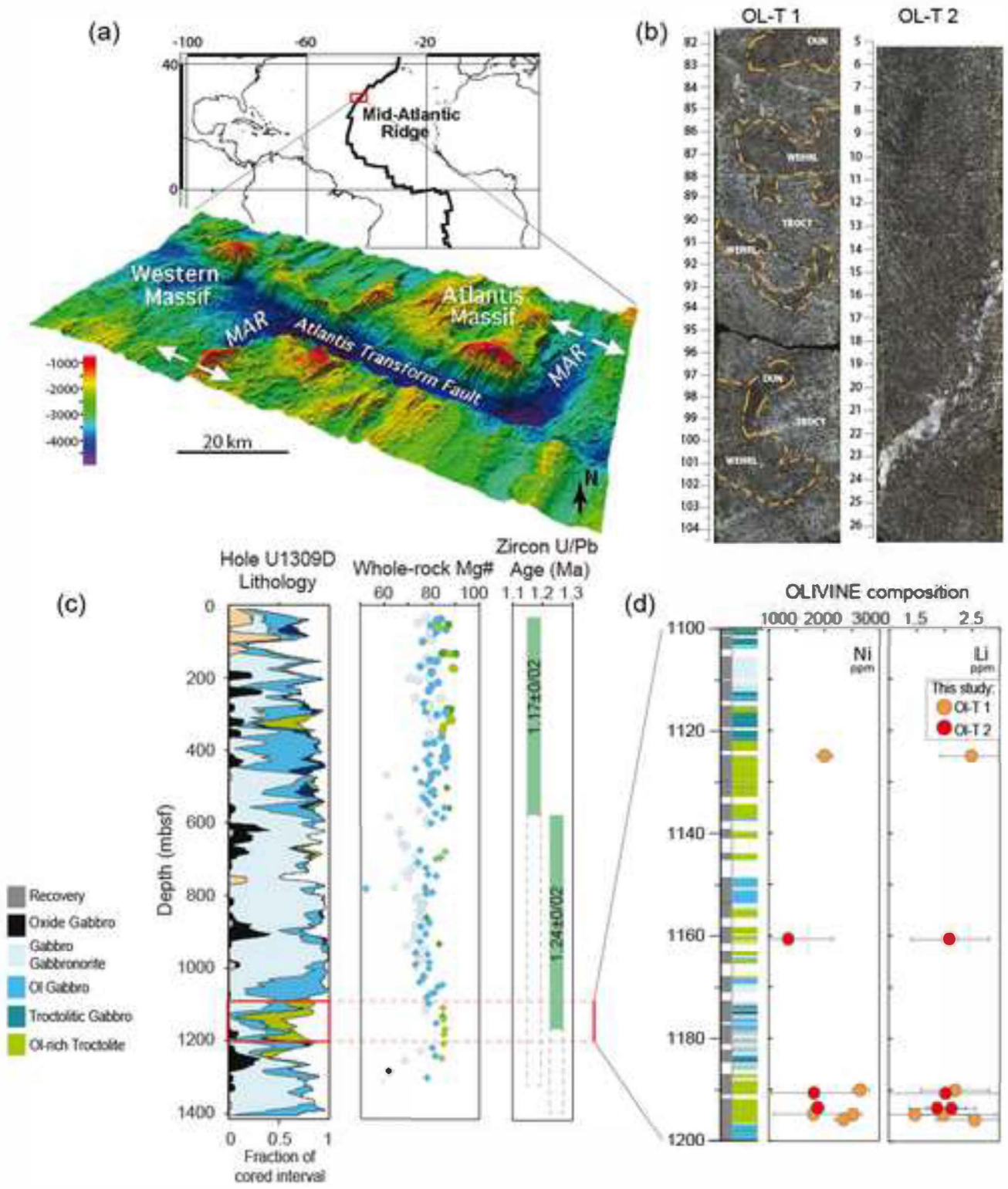
(a)
Mid-Atlantic Ridge
Western Massif
Atlantis Massif
MAR
Atlantis Transform Fault
MAR
20 km
N
(b)
OL-T 1
OL-T 2
(c)
Hole U1309D Lithology
Whole-rock Mg#
Zircon U/Pb Age (Ma)
Depth (mbsf)
Fraction of cored interval
Recovery
Oxide Gabbro
Gabbro
Gabbronorite
Ol Gabbro
Troctolitic Gabbro
Ol-rich Troctolite
(d)
OLIVINE composition
Ni ppm
Li ppm
This study:
OL-T 1
OL-T 2

Figure 2

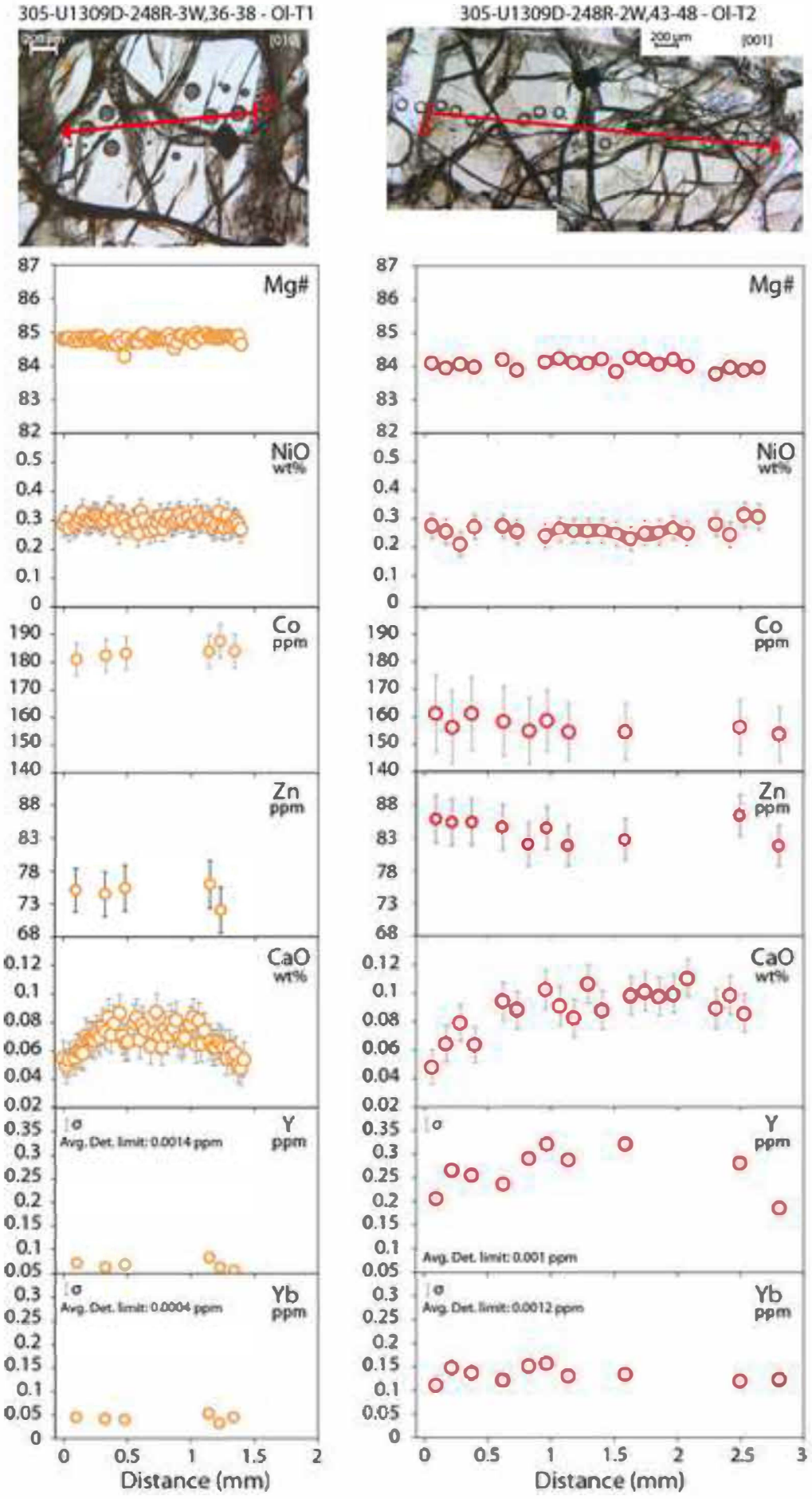
305-U1309D-248R-3W,36-38 - Ol-T1
305-U1309D-248R-2W,43-48 - Ol-T2
200 µm
[001]
Mg#
NiO wt%
Co ppm
Zn ppm
CaO wt%
Y ppm
Yb ppm
σ
Avg. Det. limit: 0.0014 ppm
Avg. Det. limit: 0.001 ppm
Avg. Det. limit: 0.0004 ppm
Avg. Det. limit: 0.0012 ppm
Distance (mm)

Figure3

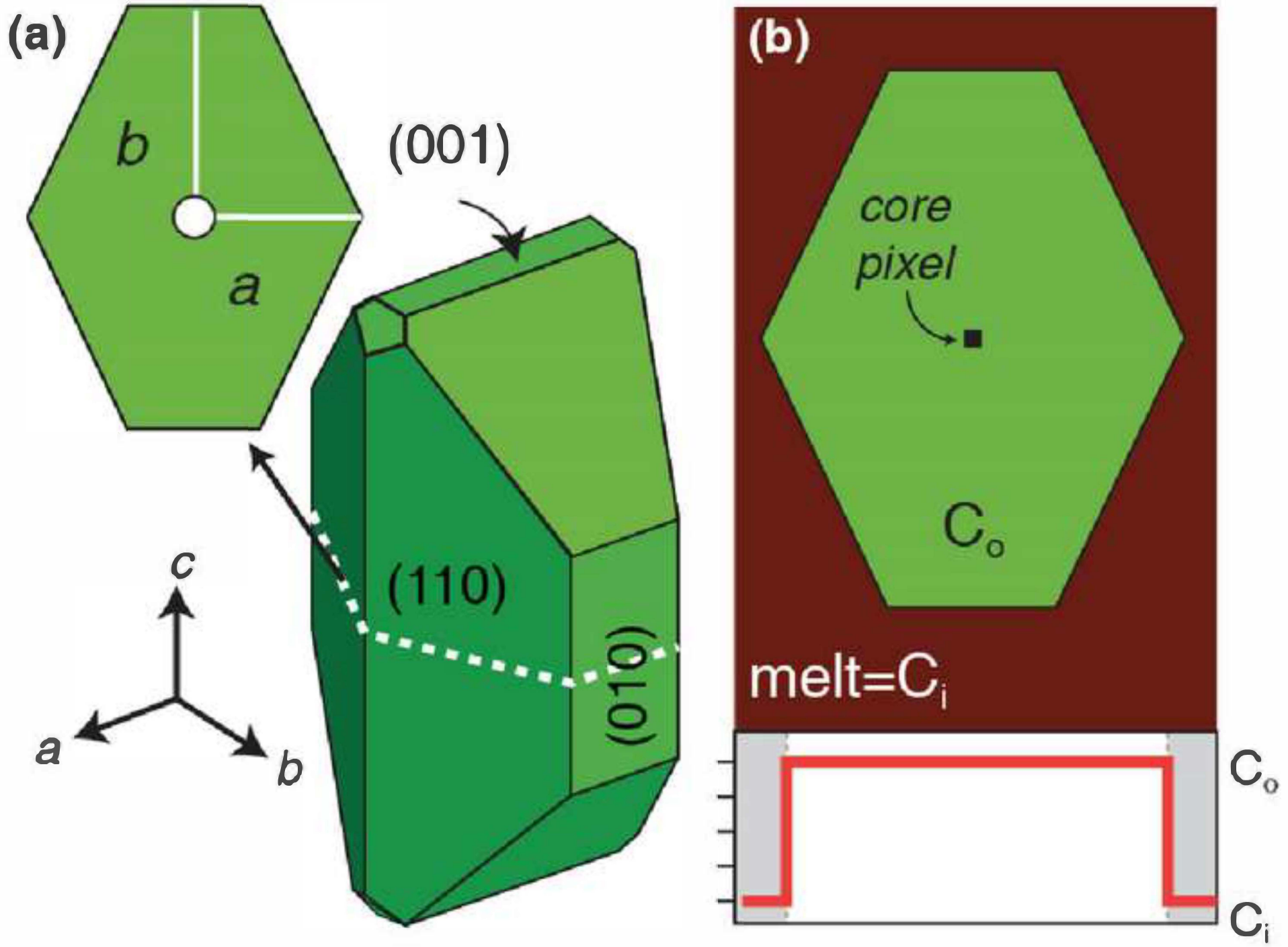

Figure4

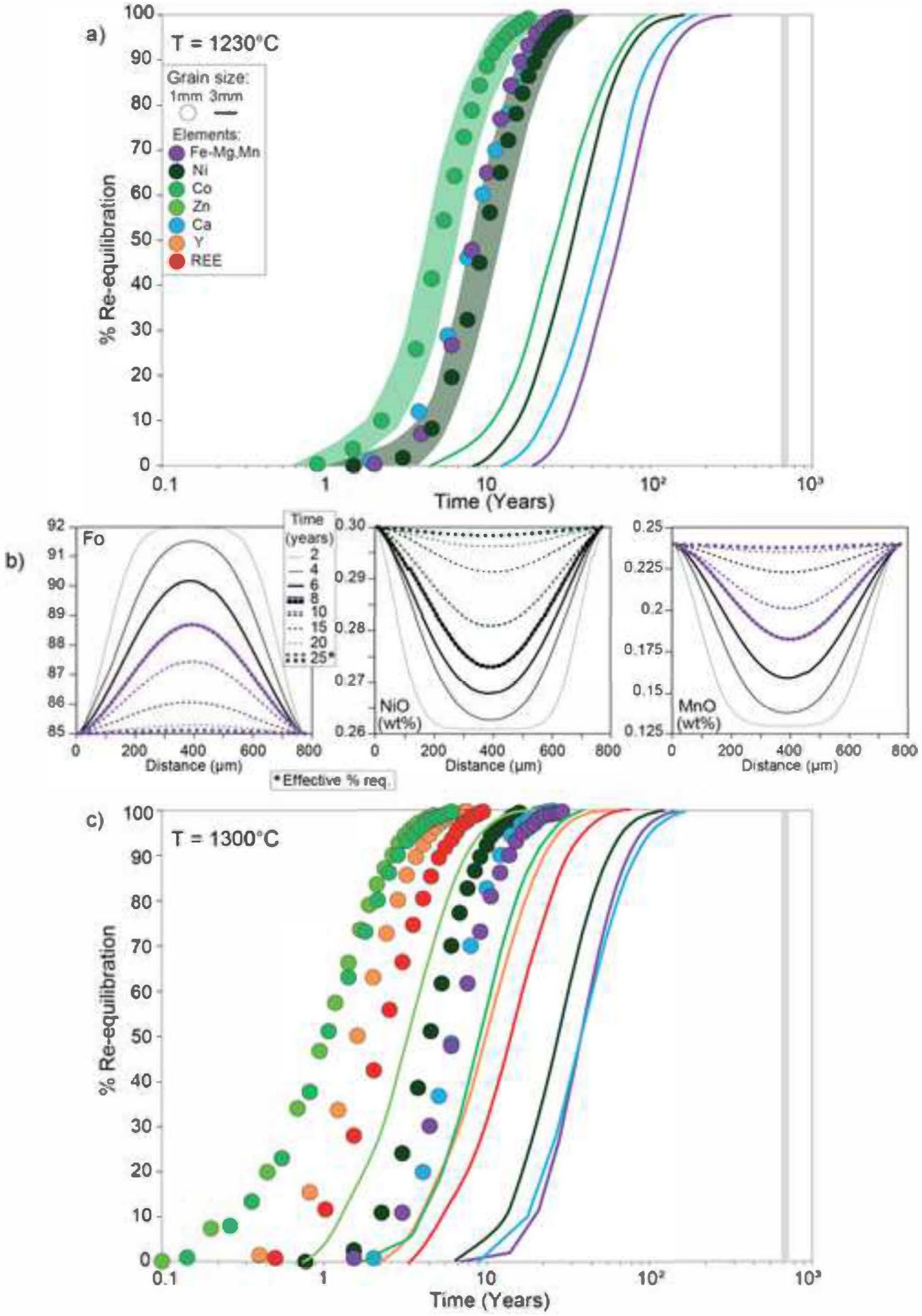
a)
T = 1230°C
Grain size:
1mm 3mm
Elements:
Fe-Mg,Mn
Ni
Co
Zn
Ca
Y
REE
% Re-equilibration
Time (Years)
b)
Fo
Time (years)
2
4
6
8
10
15
20
25*
NiO (wt%)
MnO (wt%)
Distance (μm)
*Effective % req.
c)
T = 1300°C
% Re-equilibration
Time (Years)

Figure 5

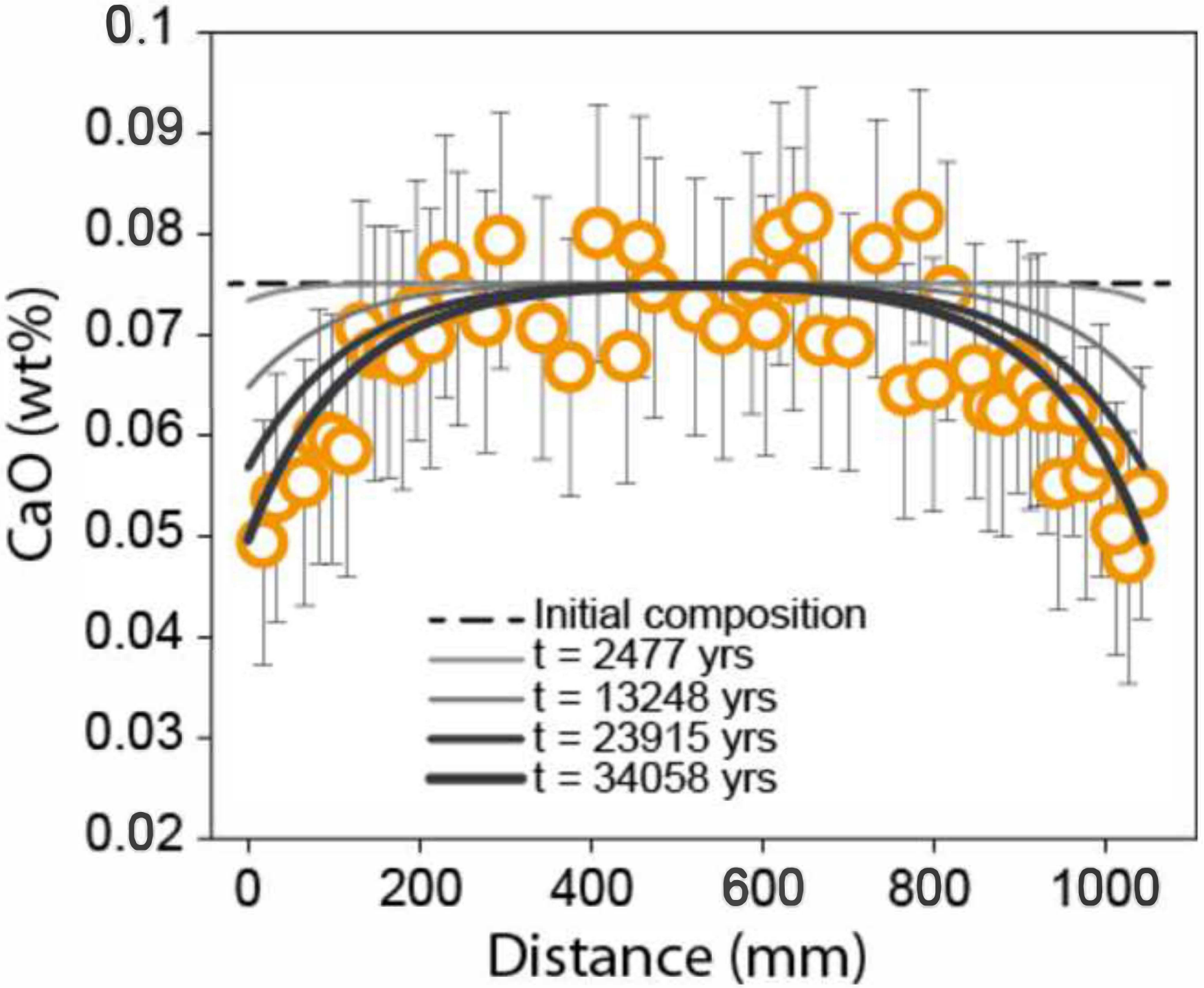
0.1
0.09
0.08
0.07
0.06
0.05
0.04
0.03
0.02
CaO (wt%)
0
200
400
600
800
1000
Distance (mm)
Initial composition
t = 2477 yrs
t = 13248 yrs
t = 23915 yrs
t = 34058 yrs

Figure6

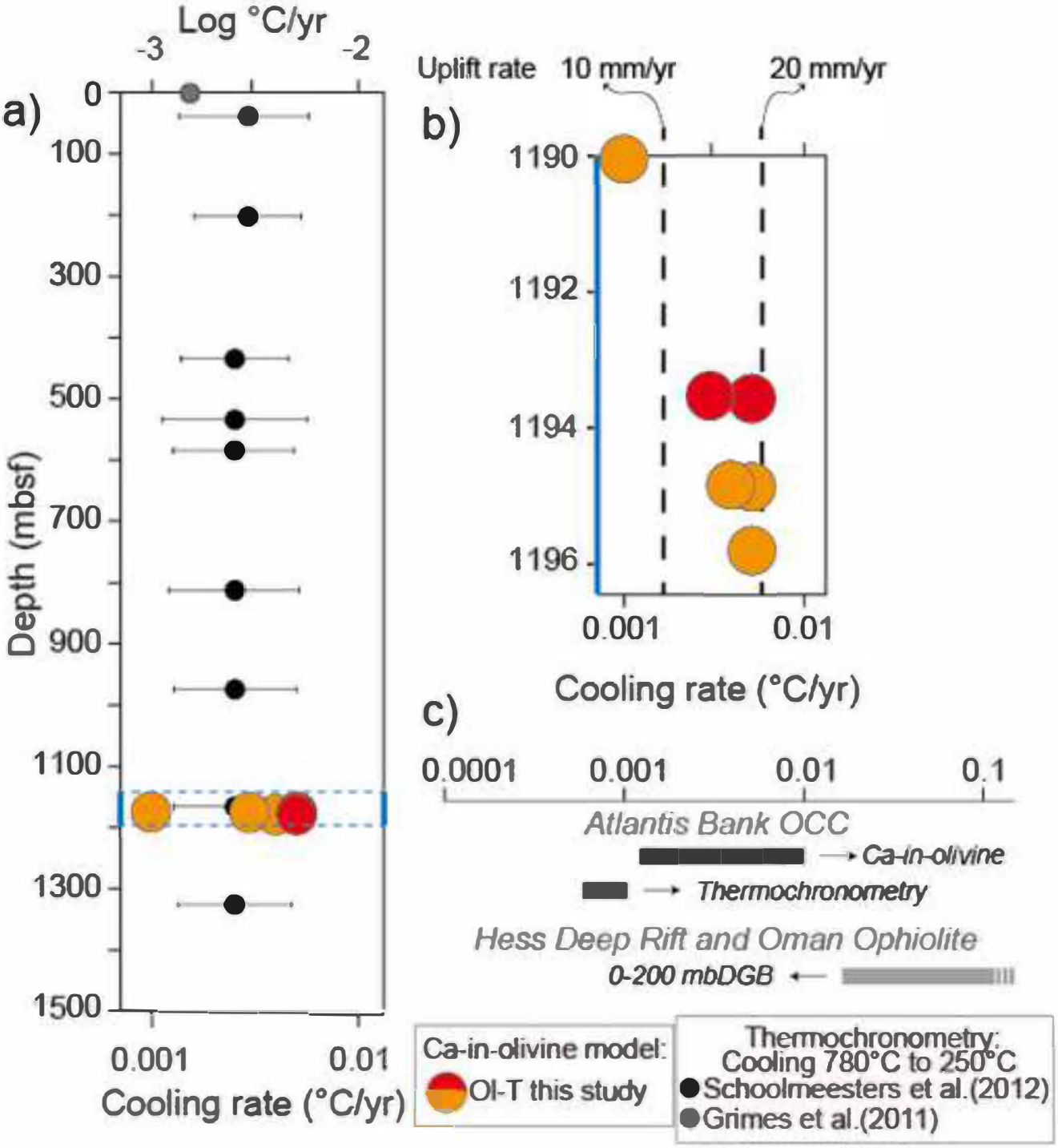
a)
Log °C/yr
-3
-2
0
100
300
500
700
900
1100
1300
1500
Depth (mbsf)
0.001
0.01
Cooling rate (°C/yr)
b)
Uplift rate 10 mm/yr
20 mm/yr
1190
1192
1194
1196
0.001
0.01
Cooling rate (°C/yr)
c)
0.0001
0.001
0.01
0.1
Atlantis Bank OCC
Ca-in-olivine
Thermochronometry
Hess Deep Rift and Oman Ophiolite
0-200 mbDGB
Ca-in-olivine model:
Ol-T this study
Thermochronometry:
Cooling 780°C to 250°C
Schoolmeesters et al.(2012)
Grimes et al.(2011)

Figure7

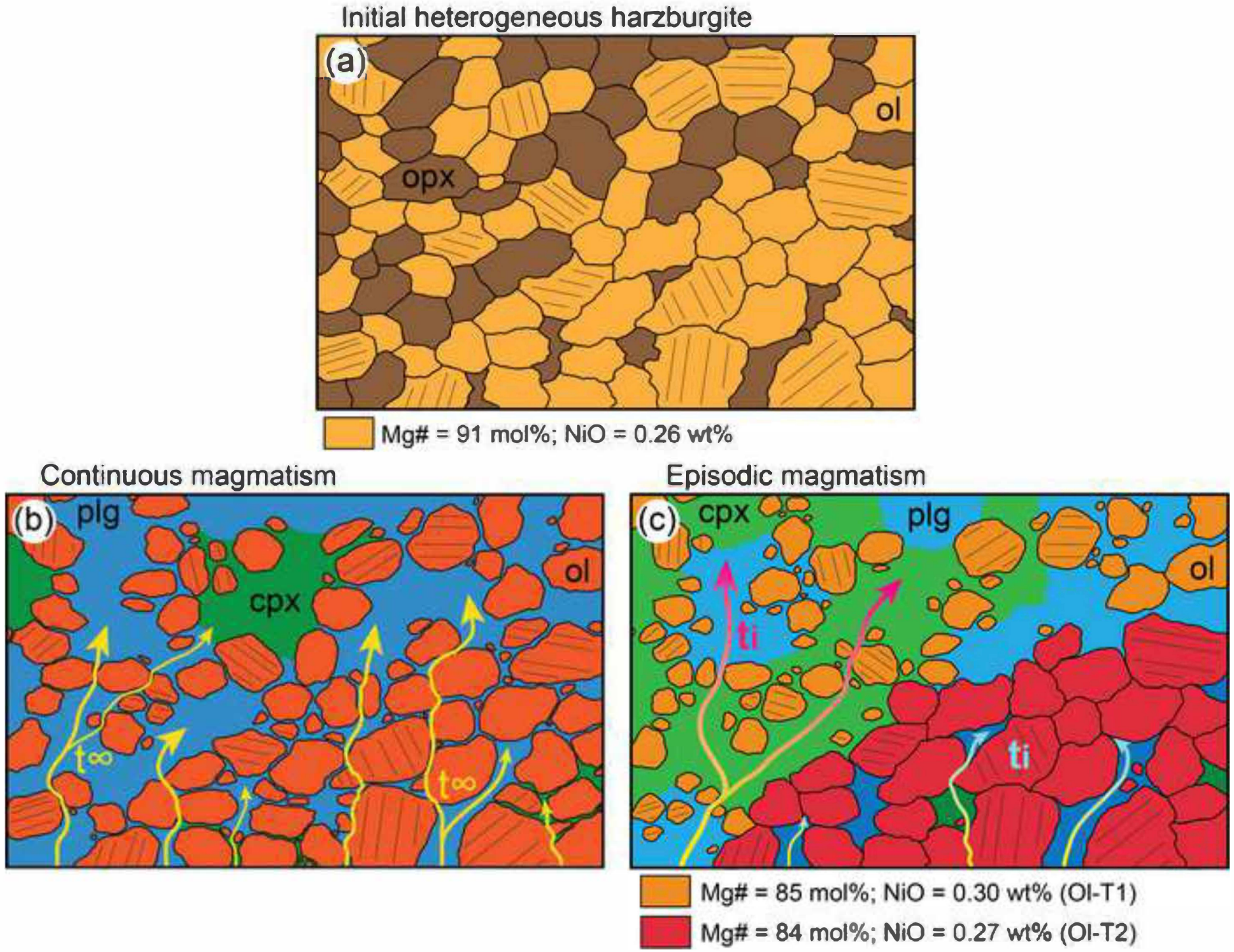
Initial heterogeneous harzburgite
(a)
ol
opx
Mg# = 91 mol%; NiO = 0.26 wt%
Continuous magmatism
(b)
plg
ol
cpx
t∞
t∞
Episodic magmatism
(c)
cpx
plg
ol
ti
ti
Mg# = 85 mol%; NiO = 0.30 wt% (Ol-T1)
Mg# = 84 mol%; NiO = 0.27 wt% (Ol-T2)

Figure8

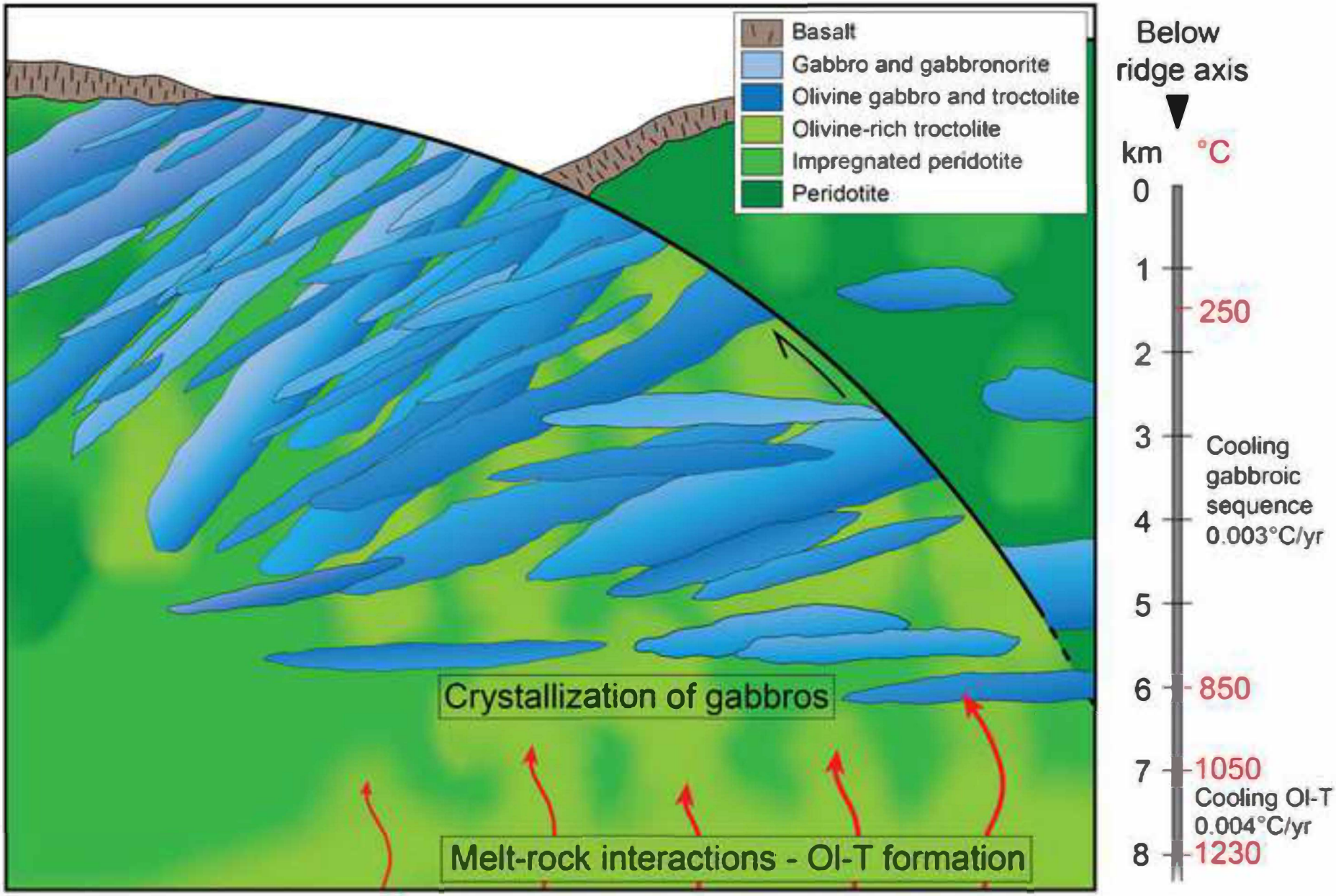
Basalt
Gabbro and gabbronorite
Olivine gabbro and troctolite
Olivine-rich troctolite
Impregnated peridotite
Peridotite
Crystallization of gabbros
Melt-rock interactions - Ol-T formation
Below ridge axis
km
°C
0
1
250
2
3
Cooling gabbroic sequence 0.003°C/yr
4
5
6
850
7
1050
Cooling Ol-T 0.004°C/yr
8
1230

Tables1,2,3

Table 1 - Selected olivine diffusion coefficients (m^2/s) reported in logarithmic scale; T ≈ 1200
([100], [010], [001] are respectively a-axis, b-axis, c-axis). [1] Dohmen et al. (2007); [2] Petry
at 1300°C; ** average between [010] and [001]; *** anisotropy not considered

	Olivine diffusion coefficients		
Elements	[100]	[010]	[001]
Fe-Mg [1]	-17.10	-17.15	-16.32
Ni [2]	-17.00	-17.02	-16.24
Co [3]			-15.41
Co [4]	-15.41	-15.35	-14.57
Zn [4] *		-14.75 **	-14.75 **
Mn [2]	-17.60	-17.57	-16.79
Ca [5]	-17.31	-16.92	-16.74
Y [4] *	-15.23	-15.22	-15.22
Lu [4] *	-15.38	-15.32	-15.32